

# Non-Abelian Reciprocal Braiding of Weyl Nodes and its Manifestation in ZrTe

Adrien Bouhon<sup>1,2,\*</sup>, QuanSheng Wu<sup>3,4,\*</sup>, Robert-Jan Slager<sup>5,\*</sup>,

Hongming Weng<sup>6,7</sup>, Oleg V. Yazyev<sup>3,4</sup>, and Tomáš Bzdušek<sup>8,9,10</sup>

<sup>1</sup>*Nordic Institute for Theoretical Physics (NORDITA), Stockholm, Sweden*

<sup>2</sup>*Department of Physics and Astronomy, Uppsala University, Box 516, SE-751 21 Uppsala, Sweden*

<sup>3</sup>*Institute of Physics, École Polytechnique Fédérale de Lausanne, CH-1015 Lausanne, Switzerland*

<sup>4</sup>*National Centre for Computational Design and Discovery of Novel Materials MARVEL, Ecole Polytechnique Fédérale de Lausanne (EPFL), CH-1015 Lausanne, Switzerland*

<sup>5</sup>*Department of Physics, Harvard University, Cambridge, MA 02138*

<sup>6</sup>*Beijing National Laboratory for Condensed Matter Physics and Institute of Physics, Chinese Academy of Sciences, Beijing 100190, China*

<sup>7</sup>*Songshan Lake Materials Laboratory, Guangdong 523808, China*

<sup>8</sup>*Condensed Matter Theory Group, Paul Scherrer Institute, CH-5232 Villigen PSI, Switzerland*

<sup>9</sup>*Department of Physics, University of Zürich, Winterthurerstrasse 190, 8057 Zürich, Switzerland and*

<sup>10</sup>*Department of Physics, McCullough Building, Stanford University, Stanford, CA 94305, USA*

(Dated: August 27, 2021)

We illustrate a procedure that transforms non-Abelian charges of Weyl nodes via braid phase factors, which arise upon exchange inside the reciprocal momentum space. This phenomenon derives from intrinsic symmetry properties of topological materials, which are increasingly becoming available due to recent cataloguing insights. Specifically, we show that band nodes in systems with  $C_2\mathcal{T}$  symmetry exhibit such braiding properties, requiring no particular fine-tuning, and we present observables in the form of generalized Berry phases, calculated via a mathematical object known as Euler form. We further extend the notion of non-Abelian topology to  $C_2\mathcal{T}$ -symmetric systems in three spatial dimensions, and investigate the interplay with the additional point-group symmetry. We find that the interaction of Euler class with mirror symmetry governs non-trivial conversions between Weyl points and nodal lines. While our findings are directly implementable in cold-atoms setups and in photonic systems via a presented braiding protocol, the predictive power of our framework is firmly underpinned by tangible material identification, namely zirconium telluride (ZrTe), which we predict to exhibit the aforementioned conversion effect under uniaxial compression strain.

Topological phases of matter constitute an active research area. The robust and illustrious properties of intrinsic topological order, such as protected edge states and the possibility of excitations that exhibit non-trivial braiding statistics [1], open up routes to potentially translate mathematical understanding of the physical phenomena to new generations of quantum technology. This has arguably also fuelled the discovery of topological band structures [2, 3] that can effectively give rise to such physical features [2–4]. The past decade has witnessed considerable progress in cataloguing topological materials [5–19], thereby providing an increasingly viable platform for bringing the potential of topological materials to experiment.

We report a concrete protocol that elucidates a novel physical phenomenon, which naturally arises from the interplay of symmetry and topology in metals and semimetals. More concretely, we show that nodal band degeneracies in systems having  $C_2\mathcal{T}$  symmetry (composition of time reversal with a  $\pi$ -rotation) are characterized by

non-Abelian frame-rotation charges. The values of these charges are transformed via non-trivial phase factors, which arise upon braiding the nodes inside reciprocal momentum space. Motivated by insights from the physics of nematic liquids [20–25] and of twisted bilayer graphene [26–32], we capture the charge transformation using generalized Berry phases, which we efficiently express using a mathematical quantity known as Euler form. Crucially, we relate our theoretical predictions to experimentally viable settings. On the one hand, we introduce a two-dimensional model that is directly implementable in cold-atom and photonic systems. Moreover, we elaborate on the interplay of the non-Abelian topology with mirror symmetry in three-dimensional systems, which entails conversions of Weyl points to nodal lines. Finally, we apply our formalism to the real-world material zirconium telluride (ZrTe) and demonstrate the node conversion effect by means of first-principles calculations.

*Three-band model and braiding protocol.*— We find that the ability of band nodes to pairwise annihilate crucially depends on the presence of band nodes in other band gaps. This enables non-trivial “reciprocal braiding” inside momentum ( $\mathbf{k}$ ) space, illustrated in Fig. 1a–b, motivating a novel partitioning of energy bands, which extends the two-fold “occupied” vs. “unoccupied” sepa-

\* These authors contributed equally. Correspondence to [adrien.bouhon@su.se](mailto:adrien.bouhon@su.se), [quansheng.wu@epfl.ch](mailto:quansheng.wu@epfl.ch), and [robert-janslager@fas.harvard.edu](mailto:robert-janslager@fas.harvard.edu).

ration. For the simplest case, namely three-band models, we introduce the following terminology. The main gap of interest, hosting the Fermi level, is called “principal gap”. Accordingly, band nodes in this gap are described as “principal nodes”. The other band gap, as well as the corresponding band and nodes, are called “adjacent”. Specifically, consider the Hamiltonian

$$H(\mathbf{k}; t) = \begin{pmatrix} f(t) & g(\mathbf{k}) & g^*(\mathbf{k}) \\ g^*(\mathbf{k}) & 0 & h(\mathbf{k}; t) \\ g(\mathbf{k}) & h^*(\mathbf{k}; t) & 0 \end{pmatrix} \quad (1)$$

with onsite energy  $f(t) = F_{[8,-]}(t)$ , couplings  $g(\mathbf{k}) = -i(e^{-ik_1\pi} - e^{-ik_2\pi})$  and  $h(\mathbf{k}; t) = h_0(t) + h_1(t)(e^{ik_1\pi} + e^{ik_2\pi})$ . Here  $h_0(t) = F_{[2,-]}(t)$  and  $h_1(t) = [10 - F_{[8,+]}(t)]$ . The dependence on the tuning parameter  $t \in [-10, 10]$  is defined through  $F_{[\nu,\pm]}(t) = \frac{1}{2}(|t + \nu| \pm |t - \nu|)$ , which is a piecewise-linear function with shoulders at  $\pm\nu$ , see Fig. 2a. The practical implementation of the model in Eq. (1) requires tuning only three tight-binding parameters, namely the potential on the first site, and the hopping amplitude between the latter two sites along horizontal resp. vertical direction. The physical degrees of freedom  $\{\phi_\alpha\}_{\alpha=A,B,C}$  are three  $s$ -wave orbitals, fulfilling  $\phi_C = C_2\phi_B$ , where the  $C_2$  rotation axis is assumed perpendicular to the basal plane. The model breaks  $C_2$  and  $\mathcal{T}$ , but preserves the combined  $C_2\mathcal{T}$  symmetry.

We realize the braiding protocol by increasing the adiabatic control parameter (“time”)  $t$  in Eq. (1) from  $-10$  to  $+10$ . The model exhibits nodal points along the diagonals of BZ,  $(1\bar{1})$  and  $(11)$ , connecting  $\Gamma$  and  $M$ . In Fig. 2c, we show snapshots of the band structure along the two diagonals during the braiding protocol with solid resp. dashed curves. The orange arrows indicate the motion of the nodal points upon increasing time. Panel Fig. 2d displays the configuration of the nodal points at a few times, keeping track of their past trajectory.

At the initial time  $t = -10$ , the bands are gapped. At  $t = -8$ , the adjacent gap exhibits a pair of nodal points moving from  $\Gamma$  (where they were created) towards  $M$  along  $(1\bar{1})$ . At  $t = -4$ , there are two principal nodes moving from  $M$  (where they were created) towards  $\Gamma$  along  $(11)$ . At  $t = -2$ , the principal nodes meet at  $\Gamma$ . Remarkably, instead of annihilating, we find that the principal nodes “bounce” in the  $(1\bar{1})$  direction, where they follow their adjacent counterparts, as visible at  $t = 0$ . Fig. 2b shows the full 2D band structure at this very time. At  $t = 2$ , the two adjacent nodes meet at  $M$  and also fail to annihilate, as can be seen at time  $t = 4$  where they progress towards  $\Gamma$ . At  $t = 8$ , the adjacent nodes have been annihilated at  $\Gamma$ . Finally, at  $t = 10$ , the principal nodes have been annihilated at  $M$ , and the bands have become fully separated again.

*Non-Abelian topology.*— The path-dependent capability of band nodes to annihilate, exemplified by the model in Eq. (1), is a consequence of underlying non-Abelian band topology. While similar phenomenon has recently been reported for nodal lines in  $\mathcal{PT}$ -symmetric sys-

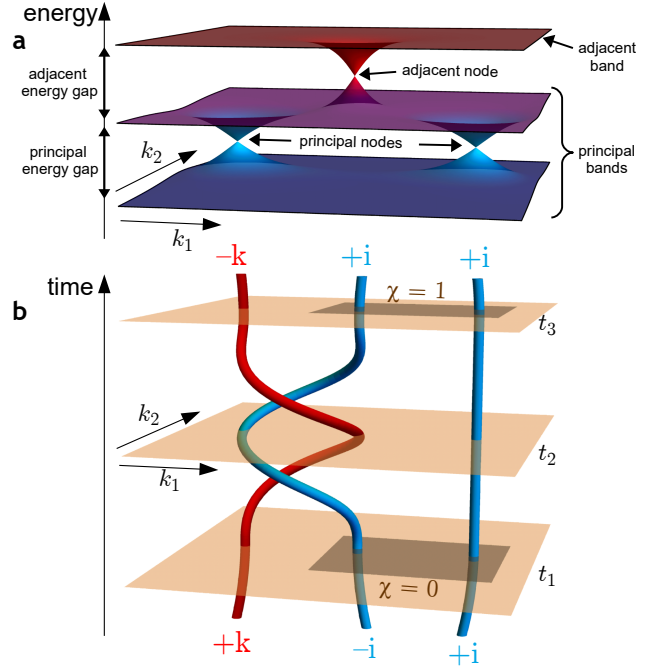


FIG. 1. **Reciprocal braiding of band nodes.** **a.** Summary of the terminology used in the text. We inspect the ability of the “principal” nodes, assumed to be near the Fermi level, to pairwise annihilate. We consider two “principal” bands that form nodal points (blue), and a third “adjacent” band which enables additional species of band nodes (red) formed among the unoccupied bands. **b.** By adjusting the Hamiltonian parameters as a function of time (orange planes  $t_{1,2,3}$ ), the node trajectories can form non-trivial braids inside the reciprocal momentum  $(k_1, k_2)$  space. The braid converts topological charges of the nodes (indicated by quaternion numbers  $\pm i$  and  $\pm k$  [25], and here dubbed “frame-rotation charges” and affects their ability to pairwise annihilate. In this work, we encode the same property using Euler class  $\chi$ , which changes value on the dark region during the braiding process. Note that the band structure in panel **a** corresponds to the situation in panel **b** at time  $t_2$ .

tems [25], we remark that point nodes are more easily experimentally studied, while also offering a more practical implementation of the braiding. Importantly, we significantly simplify the mathematical description of the non-Abelian topology. After identifying the essence of the nontrivial braid factors by encoding the underlying Hamiltonian using orthonormal frames [25], we express the capability of nodes to pairwise annihilate using the appropriate geometric concepts [30–32].

For a two-dimensional system,  $C_2\mathcal{T}$  symmetry implies the existence of a basis in which the Bloch Hamiltonian  $\mathcal{H}(\mathbf{k})$  is a *real* symmetric matrix [33]. The model in Eq. (1) is brought to this form by a unitary rotation,  $H(\mathbf{k}) \rightarrow V \cdot H(\mathbf{k}) \cdot V^\dagger$ , where  $V = \sqrt{I \oplus \sigma_x}$  [square root of the permutation matrix  $(123) \leftrightarrow (132)$ ]. Focusing on momenta where the energy bands are non-degenerate, we form an energetically ordered set of *real*  $N$  Bloch states,  $\{|u^j(\mathbf{k})\rangle\}_{j=1}^N =: F(\mathbf{k})$ , which constitutes an orthonormal frame [25]. Crucially, we assign a *frame-rotation charge* to each closed path that avoids band nodes. If one varies the momentum along a closed path based at  $\mathbf{k}_0$ , the

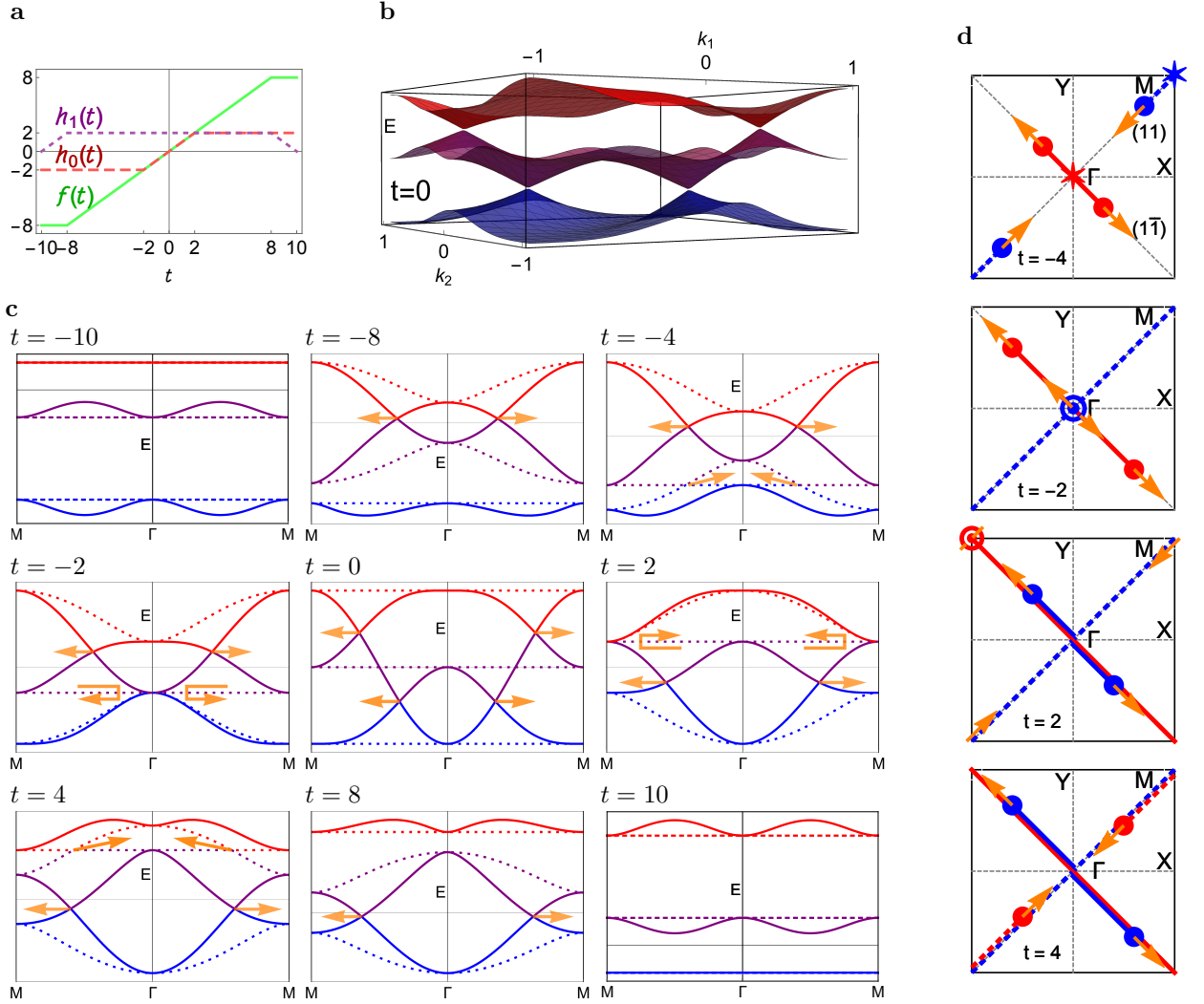


FIG. 2. **Braiding protocol defined by the model in Eq. (1).** **a.** Control parameters during the braiding protocol as a function of adiabatic time  $t$ . **b.** 2D band structure at  $t = 0$  where both principal and adjacent nodes coexist along the diagonal  $(1\bar{1})$ . **c.** Band structures along the two diagonals of the Brillouin zone (BZ), i.e.  $(1\bar{1})$  (full lines) and  $(11)$  (dashed), at successive instants of the adiabatic parameter  $t \in [-10, 10]$ . **d.** Schematic configuration of the nodal points over the 2D BZ with their past trajectory at a few instants (the dasheding matches with **c**). At  $t = -2$ , the principal nodes meet exactly at  $\Gamma$  but fail to annihilate. At  $t = 2$ , the adjacent nodes meet exactly at  $M$  without annihilating each other. The orange arrows represent the motion of the nodal points.

Hamiltonian returns to its original form. Nonetheless, the initial and the final frame at  $\mathbf{k}_0$  may differ in overall  $\pm$  sign of some eigenstates, altering the triad spanning the frame. Notably, such a transformation occurs if one encircles a band node. As one moves along a tight loop around the node formed by a pair of bands, then the two vectors describing those bands perform a  $\pi$ -rotation, while the other bands are essentially constant. This corresponds to an overall  $\pi$  rotation of the frame, related to the  $\pi$  Berry phase carried by the node [34, 35].

Given two nodes inside the same band gap, one may wonder how their associated frame rotations compose. One possibility is that the second rotation undoes the first, e.g. if we rotate by  $\pi$  in the reverse direction. In that case the two nodes annihilate when brought together. Alternatively, the rotations could revolve in the same direction. Although the total  $2\pi$ -rotation looks like a

do-nothing transformation, the Dirac's belt trick [36] reveals that a  $2\pi$ -rotation cannot be trivially undone (while a  $4\pi$  rotation can). Mathematically, this corresponds to the non-trivial fundamental group  $\pi_1[\text{SO}(N)] = \mathbb{Z}_2$  for  $N > 2$ . Physically, this implies that a pair of nodes associated with a  $2\pi$  frame rotation cannot annihilate [37].

For the three-band model in Eq. (1), we study in Fig. 3 the accumulated frame-rotation angle on two paths that enclose the two principal nodes. More precisely, we decompose the 3D rotation matrix along the path using the generators  $L_{x,y,z}$  as  $F(\mathbf{k})^\top \cdot F(\mathbf{k}_0) = \exp[\alpha L_x + \beta L_y + \gamma L_z]$ , and define the rotation angle  $\varphi = \sqrt{\alpha^2 + \beta^2 + \gamma^2}$ . As anticipated, we find that the accumulated rotation angle equals 0 ( $2\pi$ ) if the nodes can (cannot) annihilate. The difference for the two paths originates from the non-commutativity of rotations. More specifically, the rotation angle  $\alpha$  acquired as one circumnavigates

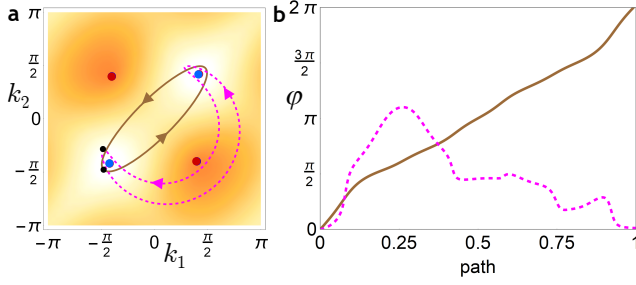


FIG. 3. **Frame-rotation charge.** **a.** The red (blue) points indicate the location inside the Brillouin zone of the principal (adjacent) nodes of the model in Eq. (1) for  $t = -4$ , cf. Fig. 2d. The shades of orange on the background indicate the magnitude of the principal gap (white denotes gapless points, darker shades mean a larger gap). The oriented solid brown resp. dashed purple lines indicate two trajectories to enclose the principal nodes, with base points  $\mathbf{k}_0$  marked with black dots. **b.** The total frame-rotation angle along the two trajectories in panel a.

a principal node is *reversed* after conjugation with the overall  $\pm\pi$  rotation associated with the adjacent node ( $e^{\pi L_j} e^{\alpha L_i} e^{\pi L_j} = e^{-\alpha L_i}$  for  $i \neq j$ ) [33]. Consequently, the topological charge of principal nodes *anticommutes* with the topological charge of the adjacent nodes. This property can be modelled by the quaternion group  $Q = \{\pm 1, \pm i, \pm j, \pm k\}$  [20, 25], as indicated in Fig. 1b.

Mathematically speaking, the orthonormal frame  $F(\mathbf{k})$  has a gauge degree of freedom, which corresponds to inverting the sign of any of the vectors. This coincides with the gauge description of the order-parameter space of a biaxial nematic [24],  $M = SO(3)/D_2$ , where  $D_2$  is the dihedral crystallographic point group. Consequently, closed paths in  $M$  are described by the fundamental group  $\pi_1[M]$  [38, 39], being the quaternion group [20–23]. It has been recognized [20] that topological defects of biaxial nematics are disclinations, which correspond to  $\pi$ -rotations around three perpendicular axes. Such defects are described by Pauli matrices, which constitute a representation of the quaternion group [38].

*Euler form.*— Although the frame-rotation angles computed in Fig. 3 faithfully predict the ability of band nodes to annihilate, the method is computationally very inefficient for many-band models. We therefore develop an alternative algorithm based on computing the *Euler form*. Here, we formally introduce Euler form, while its application to the model in Eq. (1) is presented in the next section. If  $|u^1(\mathbf{k})\rangle$  and  $|u^2(\mathbf{k})\rangle$  denote the Bloch states of the two principal bands, their Euler form is [32]

$$\text{Eu}(\mathbf{k}) = \langle \nabla u^1(\mathbf{k}) | \times | \nabla u^2(\mathbf{k}) \rangle. \quad (2)$$

The integral of Euler form over a closed surface gives an integer topological invariant called *Euler class* [30, 31]. Recently, Euler class of two occupied bands has prominently transpired in the fragile-topological characterization of twisted bilayer graphene near the magic angle [26–30]. Our work recasts this notion within stable topology of many-band models and an alternative partitioning of energy bands [33].

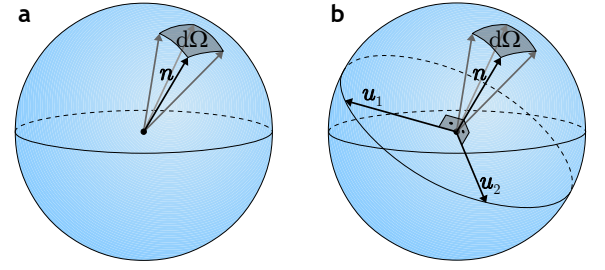


FIG. 4. **Berry curvature vs. Euler form.** **a.** For generic two-band Hamiltonians, Berry curvature corresponds to one half of the solid angle  $d\Omega$  spanned by the unit vector  $\mathbf{n}$  that encodes the Hamiltonian using the Pauli matrices. **b.** Similarly, for three-band Hamiltonians with  $C_2\mathcal{T}$  symmetry, Euler form over two bands  $\{|u_1\rangle, |u_2\rangle\}$  corresponds to the solid angle spanned by the unit vector  $\mathbf{n} = \mathbf{u}_1 \times \mathbf{u}_2$ .

Euler form and Euler class can be understood as refinements of Berry curvature and of Chern numbers [40]. We motivate this by drawing an analogy to Chern number for a two-band model  $\mathcal{H}(\mathbf{k}) = \mathbf{h}(\mathbf{k}) \cdot \boldsymbol{\sigma}$ , where  $\{\sigma_i\}_{i=1}^3$  are the Pauli matrices and  $\mathbf{h}(\mathbf{k})$  is a three-component real vector. The integral of Berry curvature over an infinitesimal domain  $dk_1 dk_2$  can be expressed [2] as one half of the solid angle

$$d\Omega = \mathbf{n} \cdot (\partial_{k_1} \mathbf{n} \times \partial_{k_2} \mathbf{n}) dk_1 dk_2 \quad (3)$$

that is covered by the unit vector  $\mathbf{n}(\mathbf{k}) = \mathbf{h}(\mathbf{k}) / \|\mathbf{h}(\mathbf{k})\|$  as  $\mathbf{k}$  ranges over the domain, cf. Fig. 4a. If momentum ranges over a *closed* manifold, then  $\mathbf{n}$  wraps around the unit sphere an integer number of times. This implies that Berry curvature integrates to integer multiples of  $2\pi$ , being the Chern number. In models with additional bands the quantization persists as shown by the theory of characteristic classes [40].

In analogy, the simplest scenario with a non-trivial Euler class over two principal bands occurs in three-band models. We find [33], as illustrated in Fig. 4b, that the integral of the Euler form over an infinitesimal domain  $dk_x dk_y$  is equal to the solid angle  $d\Omega$  in Eq. (3) (without the  $1/2$  prefactor), where  $\mathbf{n} = \mathbf{u}_1 \times \mathbf{u}_2$  is the cross product of the real three-component vectors representing the principal bands. Using arguments as before, one concludes that for three-band models the Euler form on closed manifolds integrates to integer multiples of  $4\pi$ . Although the simple geometric interpretation of the Euler form becomes insufficient in many-band models, it again follows from the theory of characteristic classes [40] that quantization persists, and

$$\chi = \frac{1}{2\pi} \oint \text{Eu}(\mathbf{k}) dk_1 dk_2 \quad (4)$$

is an integer number called the Euler class. For reasons discussed in the Supplemental Material [33], the Euler form of a pair of bands is well-defined only in the absence of adjacent nodes, while principal nodes keep the Euler form integrable [33]. We also show therein that the Euler form of real states  $|u^1\rangle$  and  $|u^2\rangle$  corresponds to the Berry



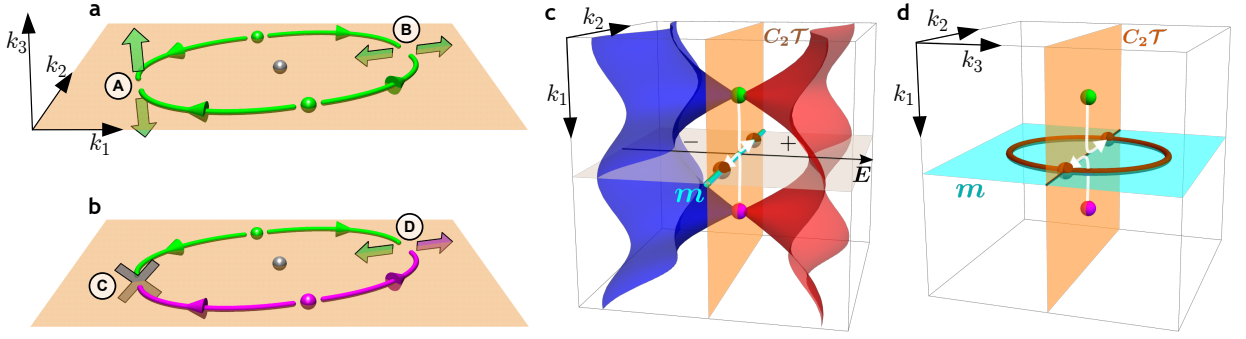


FIG. 5. **Conversion of Weyl points (WPs) in 3D momentum space.** **a.** Two principal WPs (spheres) with *equal* chirality (green color), pinned to plane  $k_3 = 0$  (orange sheet), can be brought together on two sides of an adjacent WP (grey sphere). After their collision, the two principal WPs can either symmetrically leave the plane (**A**), or remain pinned inside the plane (**B**), depending on their total frame-rotation charge. **b.** Analogous situation involving two principal WPs with *opposite* chirality (green vs. magenta color). Depending on their frame-rotation charge, the WPs either annihilate (**C**) or remain pinned inside the plane (**D**) after colliding. **c.** In the presence of an additional mirror ( $m$ ) symmetry (cyan line), the scenario (**D**) corresponds to bouncing (white arrows) of two  $m$ -related WPs to band nodes (brown spheres) lying inside  $m$ -invariant plane. This scenario occurs when the two principal bands (blue and red sheet) carry opposite eigenvalues of  $m$  (indicated by  $+$  and  $-$ ). **d.** The nodal manifold after the collision extends into a nodal line (NL, brown line) inside the  $m$ -plane (cyan sheet), which is stabilized by the mirror  $m$  symmetry. The reverse process, i.e. producing a pair of WP by colliding two NLs inside  $m \cap C_2\mathcal{T}$ , is controlled by the Euler class, see Fig. 6e for examples.

curvature of complex state  $(|u^1\rangle + i|u^2\rangle)/\sqrt{2}$ .

*Band partitioning and node diagnosis.*— To predict whether a pair of principal nodes annihilate when brought together along a specified trajectory, now assuming a system with an arbitrary number of bands, we choose a region (disk)  $\mathcal{D}$  that (i) contains the trajectory, and that (ii) does not contain any additional principal nor adjacent nodes. Note that we require the principal bands to be separated inside  $\mathcal{D}$  by an energy gap on *both* sides, i.e. from above as well as from below. Such partitioning of energy bands into three groups is in contrast with the contemporary paradigm in topological band theory [5, 6], which is to partition the bands as occupied vs. unoccupied via a single energy gap. Since the region  $\mathcal{D}$  has a boundary, the integral of the Euler form ceases to be quantized, analogous to the way Berry curvature on manifolds with a boundary does not integrate to an integer Chern number. In both cases, the quantization is restored by combining the surface integral with a contour integral of a connection over the boundary  $\partial\mathcal{D}$ , which in the present context is the Euler connection  $\mathbf{a}(\mathbf{k}) = \langle u^1(\mathbf{k}) | \nabla u^2(\mathbf{k}) \rangle$ .

Crucially, as elaborated in Supplemental Material [33], Euler connection exhibits a singularity at principal nodes, which invalidates the Stokes' theorem and prevent the cancellation of the two integrals. Specifically, we prove that the Euler class over  $\mathcal{D}$ ,

$$\chi(\mathcal{D}) = \frac{1}{2\pi} \left[ \int_{\mathcal{D}} \text{Eu}(\mathbf{k}) dk_1 dk_2 - \oint_{\partial\mathcal{D}} \mathbf{a}(\mathbf{k}) \cdot d\mathbf{k} \right], \quad (5)$$

is an integer topological invariant whenever the disk  $\mathcal{D}$  contains an *even* number of principal nodes and no adjacent nodes. If the principal nodes inside  $\mathcal{D}$  are able to collectively annihilate, this integer must be zero. This is because annihilating all the nodes makes the Euler form exact in terms of the Euler connection, i.e.  $\text{Eu} = \nabla \times \mathbf{a}$ ,

in  $\mathcal{D}$ , in which case the Stokes' theorem guarantees cancellation of the two integrals. Conversely, non-vanishing  $\chi(\mathcal{D})$  indicates an obstruction for annihilating the principal nodes. We confirm this for the model in Eq. (1) in the Supplemental Material using an algorithm detailed therein [33, 41]. There we also consider a complementary algorithm [33], which allows us to find the Euler class of a collection of principal nodes using the increasingly appreciated paradigm of Wilson-loop flows.

*Non-Abelian conversions in (3+1)D.*— We now shift our attention to three spatial dimensions. It is understood [42] that  $C_2\mathcal{T}$  symmetry can stabilize WPs *inside* high-symmetry “ $C_2\mathcal{T}$ -planes”, as observed e.g. in the  $k_z = 0$  plane of WTe<sub>2</sub> [43], MoTe<sub>2</sub> [44] and LaAlGe [45]. While such WPs are characterized by their chiral charge [9], the  $C_2\mathcal{T}$  symmetry assigns them an extra frame-rotation charge defined by the Hamiltonian inside the symmetric plane. Importantly, these charges carry complementary pieces of topological information. While the chiral charge discloses whether a pair of WPs can annihilate, the frame-rotation charge conveys whether the two WPs can disappear from the  $C_2\mathcal{T}$ -plane.

Four scenarios are possible, illustrated in Fig. 5a–b, which shows the braiding of principal WPs (marked in green vs. magenta to distinguish their chirality) around an adjacent node (gray). Starting with two WPs of equal chirality within the  $C_2\mathcal{T}$ -plane, they can either leave the plane (**A**) or bounce within the plane (**B**) when collided. Considering instead two principal WPs of opposite chirality, they can either annihilate (**C**) or bounce (**D**). In cases (**B**) and (**D**), the colliding two WPs carry a non-trivial frame-rotation charge, which obstructs their disappearance from the  $C_2\mathcal{T}$ -plane, irrespective of their chirality. In cases (**A**) and (**C**), the frame-rotation charge is trivial, allowing the pair of principal WPs to disappear from the plane.

*Interplay of Euler class with mirror symmetry.*— Ad-

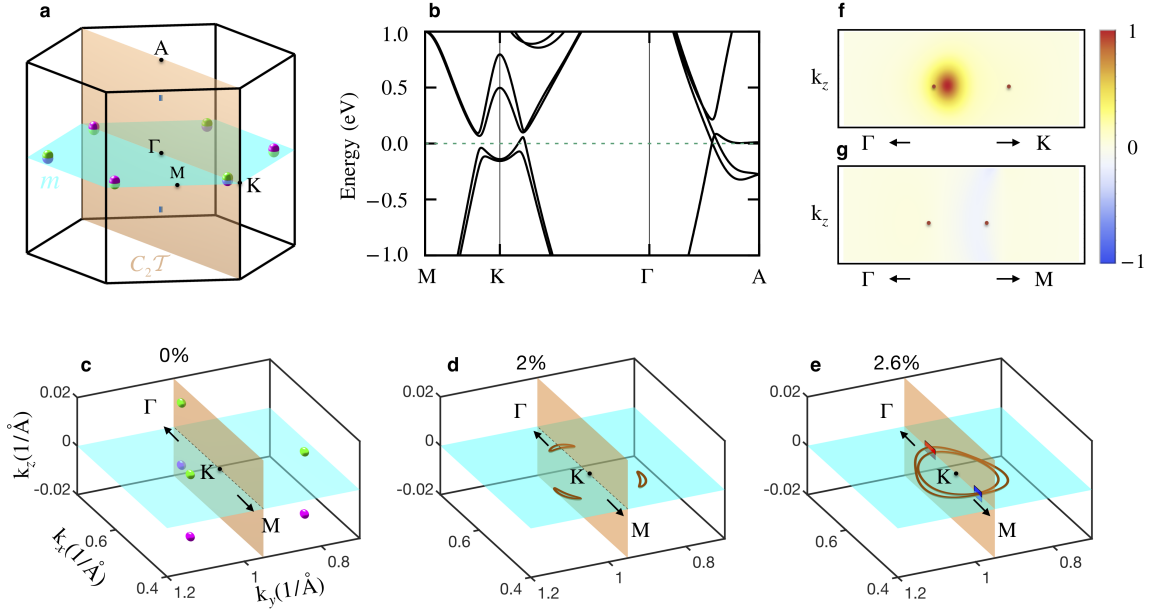


FIG. 6. **Weyl points and nodal lines in ZrTe.** **a.** The Brillouin zone (BZ) and the principal band nodes of ZrTe under ambient conditions. Weyl points (colored green resp. magenta according to their chirality) appear in pairs related by horizontal mirror  $m$ -plane (cyan), and lie within three vertical  $C_2\mathcal{T}$ -planes (one shown in orange). Four triple points, located along the  $\Gamma$ -A direction, constitute endpoints of two narrow nodal lines (blue). **b.** Band structure of ZrTe under ambient conditions. **c.** A zoom-in view of panel **a** around K point. Only one of the three vertical  $C_2\mathcal{T}$ -planes passing through the K point is displayed (orange). **d** and **e.** Nodal lines (brown) of ZrTe under 2% and 2.6% [001]-uniaxial compression strain inside the same region of BZ. **f** and **g.** Value of the Euler form, in arbitrary units as indicated by the bar diagram, inside the red resp. the blue rectangular region inside the  $C_2\mathcal{T}$ -plane of panel **e**, computed numerically using the algorithm discussed in the Supplementary Material. The Euler class [the combined surface and boundary integrals in Eq. (5)] equals 1 (non-trivial) resp. 0 (trivial) for the two regions.

ditional crystalline symmetries may interact non-trivially with the Euler class. Here, we consider the presence of a mirror symmetry  $m$ , which facilitates a mirror-invariant  $m$ -plane (cyan in Fig. 5d) perpendicular to the  $C_2\mathcal{T}$ -plane (orange in Fig. 5d). Recall that mirror symmetry can stabilize nodal-line degeneracies of bands with opposite mirror eigenvalues [10, 11].

Let us consider a WP (green in Fig. 5c) stabilized inside  $C_2\mathcal{T}$ -plane on one side of the mirror. Such a WP has a mirror-related partner of opposite chirality (magenta in Fig. 5c) on opposite side of the  $m$ -plane. Moving the two WPs together locally inverts the two bands along the intersection  $m \cap C_2\mathcal{T}$  of the two planes. We distinguish two possibilities. (1) If the two bands have the same  $m$  eigenvalue, they hybridize inside the  $m$ -plane, resulting in an avoided crossing, and the two WPs annihilate upon collision. (2) If the two bands have opposite mirror eigenvalue, they cannot hybridize. Their crossing is stable, implying that the two WPs convert to a NL [42]. Note that the resulting NL still crosses the  $C_2\mathcal{T}$ -plane at two points (brown dots in Fig. 5c), which corresponds to the “bouncing” of two nodes inside the  $C_2\mathcal{T}$ -plane (white arrows in Fig. 5d) and as described above as (D). Curiously, the fate of the reverse process, i.e. two NLs colliding inside  $m \cap C_2\mathcal{T}$ , does not uniquely follow from the relative mirror eigenvalue of the two principal bands. Nevertheless, we find that the outcome of such collisions can be predicted by computing the Euler class of the two NLs passing through the  $C_2\mathcal{T}$ -plane.

*Node conversion in ZrTe.*— Zirconium telluride (ZrTe) belonging to space group  $P\bar{6}m2$  (No. 187) is a triple-point metal with non-saturating quadratic magnetoresistance [46–49]. At ambient condition ZrTe further exhibits 6 pairs of WPs (green and magenta in Fig. 6a) related by mirror ( $m$ ) symmetry (cyan sheets in Fig. 6) near the K point of BZ, all of them lying inside vertical  $C_2\mathcal{T}$ -planes [47] (orange sheets in Fig. 6a). The WPs are located only 50 meV above the Fermi level, which could possibly be further lowered by doping. These properties make ZrTe an ideal platform to study the interplay of Euler class with crystalline symmetry.

We find, by performing first-principles computation [33, 50–52], that a 2% compressive uniaxial strain in the  $z$ -direction brings the pairs of WPs of ZrTe together at the  $m$ -plane. We remark that its relatively low Young modulus (122 GPa in the  $z$ -direction [53]) should allow for photoemission studies of ZrTe under large strains. The relative mirror eigenvalue of the two bands forming the WPs are opposite [33], hence the colliding Weyl points convert into elongated NLs (brown lines in Fig. 6d). Further increasing the strain to 2.6% fuses three elongated NLs into two concentric NL rings centered at the K point of BZ, see Fig. 6e.

The reverse process, i.e. relaxing the strain of compressed ZrTe, exhibits a collisions of two NLs within a  $C_2\mathcal{T}$ -invariant plane along both the  $\Gamma$ K as well as the KM high-symmetry lines. However, only the collisions along  $\Gamma$ K eject pairs of Weyl points, while the collision

along KM does not. We compare the two situations by computing the Euler class (5) inside the red resp. the blue rectangular regions shown in Fig. 6e, each traversed by two nodal lines, using the algorithm outlined in the Supplementary Material [33]. We find that the ejection of Weyl points from colliding NLs corresponds to a non-trivial Euler class on the rectangular region, cf. Fig. 6e and f, consistent with our theoretical predictions.

*Other experimental realizations.*— Although the ZrTe prediction underpins the predictive power of our analysis, we also mention other possible general directions. In particular, we anticipate that recent progress in the analysis of van-der-Waals heterostructures should entail an interesting research avenue. Studies into twisted bilayer graphene [26] have identified the existence of non-trivial band insulators in terms of the above characterization under  $C_2\mathcal{T}$  symmetry [27–30]. The flexibility of the stacking direction (also under stress, strain and voltage/potential differences for e.g the  $p_z$  band [27]) could potentially be utilized to realize the reciprocal braiding phenomenon in such systems. We also remark the pioneering experimental efforts to move the WPs of WTe<sub>2</sub> through  $\mathbf{k}$ -space by driving an optical “shear” phonon mode [54].

Apart from these material directions, given the concrete nature of the braiding protocol in Eq. (1), another promising direction to access this physics entails implementation in cold-atom or photonic systems. Indeed, recent experimental studies have reported techniques to measure geometric concepts related to Euler class, such as the Wilson phases [55]. Furthermore, upon the influence of an external force, elements of the Berry-Wilczek-Zee connection [56] can be obtained, and the reconstruction of Berry curvature using tomography has been experimentally achieved [57]. Similarly, photonic systems offer a platform to implement our scheme. In particular, using the waveguide setup that was recently employed to measure second Chern numbers [58], the model Hamiltonian can be realized on a 2D surface, whereas the extra  $z$ -direction acts as an adiabatic time parameter to accomplish the protocol outlined in Figs. 1 and 2.

*Conclusions.*— We presented models and protocols to uncover a non-Abelian braiding effect for momentum-space band nodes. In addition, we have presented mathematically rigorous but physically appealing analyses to characterize these phenomena by introducing the notion of Euler form, as well as Wilson-loop techniques. We emphasize that the novel vantage point reached by considering different partitionings of bands, in our case into three (rather than the usual two) sets, opens up an avenue to new theoretical and experimental studies, as it allows for more intricate topological structures [25]. The discussed models and phenomena are within current experimental reach, and the predictive power of our framework is reflected in a specific material example.

*Acknowledgements.*— We acknowledge valuable discussions with C. C. Wojcik, A. Vishwanath, and B. A. Bernevig. R.-J. S acknowledges funding via A. Vishwanath from the Center for Advancement of Topological Semimetals, an Energy Frontier Research Center funded by the U.S. Department of Energy Office of Science, Office of Basic Energy Sciences, through the Ames Laboratory under its Contract No. DE-AC02-07CH11358. T. B. was supported by the Gordon and Betty Moore Foundation’s EPiQS Initiative, Grant GBMF4302, and by the Ambizione Program of the Swiss National Science Foundation. Q.-S. W and O.V.Y acknowledge support from NCCR Marvel. H.M.W acknowledge support from the Ministry of Science and Technology of China under grant numbers 2018YFA0305700, 2016YFA0300600. First-principles calculations have been performed at the Swiss National Supercomputing Centre (CSCS) under Project No. s832 and the facilities of Scientific IT and Application Support Center of EPFL.

*Author Contributions.*— A. B., R.-J. S., and T. B. contributed equally to the theoretical analysis in this work, and wrote the manuscript. Q.-S. W. discovered the nodal conversion in ZrTe, and obtained the presented first-principles data. H.M. W. and O. V. Y. were involved in the discussion and analysis of the first-principles data. All authors discussed and commented on the manuscript.

## LIST OF CONTENTS

This document contains supplemental information, which has been omitted from the main text to keep it brief and simple. We have organized the information into sections, as follows:

- A. **Tight-binding models and numerical results.** 1  
We discuss additional details of the three-band tight-binding model and braiding protocol discussed in the main text.
- B. **Reality condition.** 2  
We show that the existence of antiunitary symmetry squaring to  $+1$  implies the existence of a basis in which the Bloch Hamiltonian becomes a real symmetric matrix.
- C. **Euler form and Euler class** 2  
We introduce the notion of Euler form and Euler class for orientable real vector bundles on closed manifolds, and emphasize the analogy with the first Chern number. We also relate Euler form of two real Bloch states to Berry curvature of one complexified state.
- D. **Euler form in three-band models.** 5  
We prove the geometric interpretation of the Euler form in three-band models, which is presented in Fig. 4(b) of the main text.
- E. **Analytic properties of Euler form at principal nodes.** 6  
We study analytic properties of Euler form and Euler connection near principal nodes. We find that Euler form is continuous and integrable at principal nodes. However, if the calculation is done in the eigenstate basis, the Euler connection diverges at principal nodes, which poses an obstruction for the naïve application of Stokes' theorem.
- F. **Euler class for manifold with a boundary.** 10  
We generalize Euler class to manifolds with a boundary, and we show that it detects the capability of pairs of principal nodes to annihilate.
- G. **Non-Abelian frame-rotation charge.** 11  
We review the homotopic derivation of the non-Abelian frame-rotation charge from Ref. [25], and we prove its relation to the Euler class on manifolds with a boundary.
- H. **Numerical calculation of the Euler form.** 13  
We present a numerical algorithm that calculates the Euler class on a manifold with a boundary. The algorithm employs the complexification trick from Sec. C 4.
- I. **Frame rotations vs. flow of the Pfaffian** 15  
We present an efficient computation of the frame-rotation charge (Euler class) of a pair of principal nodes through the winding of Wilson loop over the punctured Brillouin zone excluding the adjacent nodes.
- J. **First-principle calculations** 16  
We present additional details concerning our modelling of ZrTe with and without strain using first-principles calculations



## A. Tight-binding models and numerical results

### 1. Generic tight-binding model

We derive a generic three-dimensional three-band tight-binding model with the single constraint that it satisfies  $C_2\mathcal{T}$  symmetry with  $(C_2\mathcal{T})^2 = +1$ , and given a choice of the Wyckoff positions.  $C_2\mathcal{T}$  symmetry requires the magnetic space group  $P12'_1$  (#3.3.10) as minimal subgroup [59, 60], i.e. the direct product between the primitive monoclinic Bravais lattice as the normal subgroup of translations and the magnetic point group  $2' = \{E, C_2\mathcal{T}\}$  (#3.3.8) with  $\hat{y}$  as the  $C_2$  rotation axis [59, 60].

We choose the primitive lattice vectors as  $\mathbf{a}_1 = a(\sin\theta, 0, \cos\theta)$ ,  $\mathbf{a}_2 = b(1, 0, 0)$ , and  $\mathbf{a}_3 = c(0, 1, 0)$ , and write their dual (primitive reciprocal lattice vectors) as  $\{\mathbf{b}_1, \mathbf{b}_2, \mathbf{b}_3\}$  ( $\mathbf{a}_i \cdot \mathbf{b}_j = 2\pi\delta_{ij}$ ) taken as the basis for the Bloch wave vector (momentum)  $\mathbf{k} = (k_1\mathbf{b}_1 + k_2\mathbf{b}_2 + k_3\mathbf{b}_3)/2$ . Note that the  $C_2$  rotation axis ( $\hat{y}$  as in [59]) is  $\mathbf{a}_3$  in our basis, i.e. it acts component-wise on the momentum as  $C_2(k_1, k_2, k_3) = (-k_1, -k_2, k_3)$ . The  $C_2$  rotation axis defines a basal plane perpendicular to it.

The advantage of the crystallographic convention ( $C_2$  taken along  $\hat{y}$ ) is that if we choose  $\hat{z}$  as the quantization axis for the spin, the representation of  $C_2^{(\hat{y})}\mathcal{T}$  symmetry on the pure spinor basis  $(\phi_\uparrow, \phi_\downarrow)$  takes the simple form  $(-i\sigma_y)(i\sigma_y\mathcal{K}) = \mathbf{1}\mathcal{K}$  (where  $\mathcal{K}$  is complex conjugation), i.e. it makes explicit the fact that it acts trivially on the spin degrees of freedom. As a consequence, our model below holds both for spinful and spinless systems, since it is constrained only by  $C_2\mathcal{T}$  symmetry. From now on we thus discard spin indices and remark explicitly when a statement is only valid for the spinless case.

In the following we make the assumption that one real  $s$ -wave orbital sits on Wyckoff's positions  $1b$  and  $2e$  [59]. Since  $2e$  is twofold ( $1b$  is invariant under  $C_2$ ,  $2e$  is not) there are three sub-lattice sites per unit cell. We take their locations within the  $n$ -th unit cell as  $\{\mathbf{R}_n + \mathbf{r}_\alpha\}_{\alpha=A,B,C}$ , with  $\mathbf{r}_A = (0, 0, 0)$  for  $1b$ , and  $\mathbf{r}_B = (u, v, w)$  and  $\mathbf{r}_C = (-u, -v, w)$  for  $2e$  (here and in the following we write all vectors of the direct space in the primitive basis  $\{\mathbf{a}_i\}_{i=1,2,3}$ ). We write the localized Wannier function for the  $\alpha$ -th orbital of the  $n$ -th unit cell as  $|w, \mathbf{R}_n + \mathbf{r}_\alpha\rangle$ . The Bloch basis is then given through the discrete Fourier transform as

$$|\varphi_\alpha, \mathbf{k}\rangle = \frac{1}{\sqrt{N_\alpha}} \sum_{\mathbf{R}_n} e^{i\mathbf{k} \cdot \mathbf{R}_n} |w, \mathbf{R}_n + \mathbf{r}_\alpha\rangle, \quad \alpha = A, B, C, \quad (1)$$

with  $N_\alpha$  the number of lattice sites with an  $\alpha$ -orbital. In the following we use the row vector notation  $|\varphi, \mathbf{k}\rangle = (|\varphi_A, \mathbf{k}\rangle \mid |\varphi_B, \mathbf{k}\rangle \mid |\varphi_C, \mathbf{k}\rangle)$ .  $C_2\mathcal{T}$  symmetry acts then as

$$C_2\mathcal{T}|\varphi, \mathbf{k}\rangle = |\varphi, (k_1, k_2, -k_3)\rangle(1 \oplus \sigma_x)\mathcal{K}. \quad (2)$$

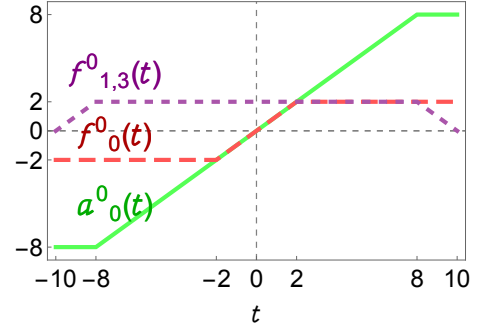


FIG. S-1. Tight-binding parameters of the 2D minimal model as functions of the control parameter  $t$ .

We can now write the Bloch tight-binding model

$$\mathcal{H} = \sum_{\mathbf{k} \in \text{BZ}} |\varphi, \mathbf{k}\rangle H(\mathbf{k}) \langle \varphi, \mathbf{k}|, \quad (3)$$

with the matrix components

$$H_{\alpha\beta}(\mathbf{k}) = \sum_{\mathbf{n} \in \mathbb{N}^3} T_{\alpha\beta}(\mathbf{n}) e^{i\mathbf{k} \cdot (n_1\mathbf{a}_1 + n_2\mathbf{a}_2 + n_3\mathbf{a}_3)}, \quad (4)$$

where the Bloch wave vector  $\mathbf{k} = (k_1\mathbf{b}_1 + k_2\mathbf{b}_2 + k_3\mathbf{b}_3)/2$  is taken within the first Brillouin zone (BZ), i.e.  $(k_1, k_2, k_3) \in (-1, 1]^{\times 3}$ .

The hopping parameters  $T_{\alpha\beta}(\mathbf{n}) \in \mathbb{C}$  are constrained by symmetry. First of all, hermiticity imposes

$$T_{\beta\alpha}(\mathbf{n}) = T_{\alpha\beta}(-\mathbf{n})^*. \quad (5)$$

Then,  $C_2\mathcal{T}$  requires

$$(1 \oplus \sigma_x) H^*(k_1, k_2, k_3) (1 \oplus \sigma_x) = H(k_1, k_2, -k_3), \quad (6)$$

which can be recast into constraints

$$\begin{aligned} T_{AA}(C_2\mathbf{n}) &= T_{AA}(\mathbf{n})^*, & T_{AC}(C_2\mathbf{n}) &= T_{AB}(\mathbf{n})^*, \\ T_{CC}(C_2\mathbf{n}) &= T_{BB}(\mathbf{n})^*, & T_{CB}(C_2\mathbf{n}) &= T_{BC}(\mathbf{n})^*. \end{aligned} \quad (7)$$

In the following we choose the parameters  $\{T_{BA}(\mathbf{n}), T_{BC}(\mathbf{n}), T_{CA}(\mathbf{n}), T_{AC}(\mathbf{n}), T_{CC}(\mathbf{n})\}$  as functions of the other parameters, respecting Eqs. (5) and (7).

### 2. Minimal 2D model

We define here the 2D minimal model discussed in the main text in terms of the generic tight-binding model introduced above. Since it lies within the basal plane only, we have  $p_j^{u,d} = 0$  for all  $j$ . Then, among the basal tight-binding terms only the following are set to finite values  $\{a_0^0, d_5^0, d_7^0, f_0^0, f_1^0, f_3^0\}$ .

Introducing the parameter  $t$  that controls the braiding and using the notations of the main text, we obtain the

minimal model

$$H_{2D}(\mathbf{k}; t) = \begin{pmatrix} f(t) & g(\mathbf{k}) & g^*(\mathbf{k}) \\ g^*(\mathbf{k}) & 0 & h(\mathbf{k}; t) \\ g(\mathbf{k}) & h^*(\mathbf{k}; t) & 0 \end{pmatrix}, \quad (8)$$

where

$$\begin{aligned} f(t) &= a_0^0(t), \\ g(\mathbf{k}) &= d_5^0 e^{-ik_1\pi} + d_7^0 e^{-ik_2\pi}, \\ h(\mathbf{k}; t) &= f_0^0(t) + f_1^0(t) e^{ik_1\pi} + f_3^0(t) e^{ik_2\pi}, \end{aligned} \quad (9)$$

and

$$\begin{aligned} a_0^0(t) &= F_{[8,-]}(t), & f_0^0(t) &= F_{[2,-]}(t) \\ d_5^0 &= -i, & f_1^0(t) &= 10 - F_{[8,+]}(t), \\ d_7^0 &= i, & f_3^0(t) &= f_1^0(t), \end{aligned} \quad (10)$$

with the  $t$ -dependent functions defined through  $F_{[\rho,\pm]}(t) = 1/2(|t + \nu| \pm |t - \nu|)$ , see Fig. S-1.

Importantly, the overly simplified form of the minimal model leads to an effective auxiliary  $C_2$  symmetry

$$U(1 \oplus \sigma_x) H(C_2 \mathbf{k}) (1 \oplus \sigma_x) U^\dagger = H(\mathbf{k}), \quad (11)$$

with  $U = \text{diag}(-1, 1, 1)$  corresponding to the gauge transformation  $\phi_A \rightarrow -\phi_A$ . This can be straightforwardly verified from the explicit expressions Eq. (8) and (9).

As a consequence of this effective symmetry, the band structure is  $C_2$  symmetric and Weyl points (WPs) can only be created four at a time, i.e. two pairs of WPs with opposite chirality. Indeed, any WP at  $\mathbf{k}$  must have its symmetric partner of equal chirality at  $C_2 \mathbf{k}$ , and these must have their symmetric partners of opposite chirality at  $-C_2 \mathbf{k}$  and  $-\mathbf{k}$  due to  $C_2 \mathcal{T}$  symmetry. This property is relaxed in the model used for the 3D protocol of the main text, see Section A7.

## B. Reality condition

In the main text, we assumed that  $C_2 \mathcal{T}$  symmetry automatically implies reality of the Bloch Hamiltonian. While this is not true in general, the conclusions presented in the main text still apply. More precisely, the existence of antiunitary operator  $\mathcal{A}$  that obeys (i)  $\mathcal{A}^2 = +1$  and (ii)  $\forall \mathbf{k} : \mathcal{A} \mathcal{H}(\mathbf{k}) \mathcal{A}^{-1} = \mathcal{H}(\mathbf{k})$ , implies the existence of a Hilbert-space basis, in which the Hamiltonian  $\mathcal{H}(\mathbf{k})$  is real. In this section we justify this claim by two different methods. We remark that the antiunitary  $\mathcal{A}$  that fulfills the two conditions can be realized as  $C_2 \mathcal{T}$  in two-dimensional spinful or spinless systems [31], or as  $\mathcal{PT}$  in spinless systems of arbitrary dimension [25]. Therefore, for such symmetry settings, both the frame-rotation charge resp. the Euler can be defined if the right Hilbert-space basis has been adopted.

We first prove this statement formally, before providing

a physical insight in the next paragraph. Every antiunitary operator  $\mathcal{A}$  can be represented as some unitary operator  $\mathcal{U}$  composed with the complex conjugation  $\mathcal{K}$  [61], i.e.  $\mathcal{A} = \mathcal{U} \mathcal{K}$ . Unitarity means that  $\mathcal{U} \mathcal{U}^\dagger = 1$ , while  $\mathcal{A}^2 = +1$  implies that  $\mathcal{U} \mathcal{U}^* = 1$ . It follows that  $\mathcal{U} = \mathcal{U}^\top$ . The Autonne-Takagi factorization [62] then guarantees that  $\mathcal{U} = \mathcal{V} \mathcal{D} \mathcal{V}^\top$  for some unitary  $\mathcal{V}$  and a diagonal matrix  $\mathcal{D} = \text{diag}\{e^{i\varphi_j}\}_{j=1}^n$ . Constructive and finite algorithms exist that find the Autonne-Takagi decomposition of a symmetric unitary matrix [63]. Rotation of the Hilbert-space by unitary matrix  $\sqrt{\mathcal{D}^*} \mathcal{V}^\dagger \equiv \mathcal{W}$  then transform the antiunitary operator to  $\mathcal{W} \mathcal{A} \mathcal{W}^\dagger = \mathcal{K}$ , i.e. to the form assumed in the main text.

From a physical point of view, it is well known that an antiunitary symmetry squaring to  $+1$  (rather than  $-1$ ) does *not* imply Kramers degeneracies [64]. In other words, eigenstates of  $\mathcal{A}$  form generally one-dimensional irreducible representations for this symmetry. By taking these eigenstates to form the basis of the Hilbert space, the antiunitary operator is represented by  $\mathcal{D}' \mathcal{K}$ , where  $\mathcal{D}' = \text{diag}\{e^{i\varphi_j'}\}_{j=1}^n$  is a diagonal matrix of phase factors. Rotating the Hilbert space basis by  $\mathcal{W}' = \sqrt{\mathcal{D}'^*}$  then transforms the antiunitary operator to just the complex conjugation  $\mathcal{K}$ . While the absence of Kramers doubling for such a symmetry is well accepted in the solid-state community, the formal proof of this statement actually follows from the Autonne-Takagi factorization, as discussed in the previous paragraph.

## C. Definition of Euler form and Euler class

In this section, we outline the mathematical definition of Euler form and of Euler class for real vector bundles. To make the analogy with the Berry curvature and Chern number manifest, we first review the definitions and the properties of these more familiar objects. Note that in this section we adopt the language of differential forms [65], since it allows for more concise expression of the studied objects and of the relations between them.

### 1. General vector bundles

We first recall the basic terminology. A collection of  $n$  bands over a base space  $B$  defines an  $n$ -dimensional vector bundle  $E \rightarrow B$ , which is generically *complex*. In this section we assume that the vector bundle is *smooth* (although this assumption would be lifted in later sections, in particular Sec. E). We order the states  $\{|u^a(\mathbf{k})\rangle\}_{a=1}^n$  as columns into a rectangular matrix  $\mathcal{U}(\mathbf{k})$ , and we construct the Berry-Wilczek-Zee (BWZ) connection [56]

$$\mathcal{A}(\mathbf{k}) = \mathcal{U}^\dagger(\mathbf{k}) d\mathcal{U}(\mathbf{k}), \quad (12)$$

where “ $d$ ” is the exterior derivative (i.e. the differentiation  $d = dk^i \partial_{k_i}$  followed by antisymmetrization in covariant indices [65]). Mathematically,  $\mathcal{A}(\mathbf{k})$  is a 1-form

with values in Lie algebra  $\mathfrak{u}(n)$ . At the level of individual components, the connection can be expressed as

$$\mathcal{A}_i^{ab}(\mathbf{k}) = \langle u^a(\mathbf{k}) | \partial_{k_i} u^b(\mathbf{k}) \rangle, \quad (13)$$

where  $i$  is a momentum component (the 1-form part), and  $a, b$  are band indices (the Lie algebra part). This object is skew-Hermitian in band indices because the Lie algebra  $\mathfrak{u}(n)$  corresponds to skew-Hermitian matrices. Mixing the  $n$  states with a matrix  $X(\mathbf{k}) \in \mathbf{U}(n)$  as  $\tilde{\mathcal{U}}(\mathbf{k}) = \mathcal{U}(\mathbf{k})X(\mathbf{k})$ , i.e. performing a *gauge transformation*, transforms the connection as

$$\tilde{\mathcal{A}} = X^\dagger \mathcal{A} X + X^\dagger dX, \quad (14)$$

where we dropped the momentum arguments for brevity.

The BWZ *curvature* is defined as

$$\mathcal{F} = d\mathcal{A} + \mathcal{A} \wedge \mathcal{A}. \quad (15)$$

Mathematically, this is a 2-form with values in  $\mathfrak{u}(n)$ . Componentwise,

$$\begin{aligned} \mathcal{F}_{ij}^{ab} = & \langle \partial_{k_i} u^a | \partial_{k_j} u^b \rangle - \langle \partial_{k_j} u^a | \partial_{k_i} u^b \rangle, \\ & + \langle u^a | \partial_{k_i} u^c \rangle \langle u^c | \partial_{k_j} u^b \rangle - \langle u^a | \partial_{k_j} u^c \rangle \langle u^c | \partial_{k_i} u^b \rangle \end{aligned} \quad (16)$$

which is skew-symmetric in momentum coordinates (the 2-form part), and skew-Hermitian in band indices (the Lie algebra part). The curvature transforms covariantly under gauge transformations,

$$\tilde{\mathcal{F}} = X^\dagger \mathcal{F} X \quad (17)$$

which allows us to define a gauge-invariant object,  $\mathbf{F} = -i \text{tr}(\mathcal{F})$ , usually called *Berry curvature*. The trace in this definition runs over band indices, i.e. we perform a projection  $\mathfrak{u}(n) \rightarrow \mathfrak{u}(1)$ . Assuming the Einstein summation convention, this amounts to

$$\mathbf{F}_{ij} = -i \mathcal{F}_{ij}^{aa} = -i (\langle \partial_{k_i} u^a | \partial_{k_j} u^a \rangle - \langle \partial_{k_j} u^a | \partial_{k_i} u^a \rangle) \quad (18)$$

where the two terms in the second line of Eq. (16) have cancelled each other. One can similarly define *Berry connection*  $A = \text{tr} \mathcal{A}$ . Since the expression  $[\mathcal{A} \wedge \mathcal{A}]_{ij} = A_i A_j - A_j A_i$  in Eq. (15) has zero trace, it follows that  $\mathbf{F} = dA$ .

## 2. Real vector bundles

We now switch gears and discuss the Euler connection and Euler form. We adopt the reality condition from Sec. B and the real gauge for the states  $|u^a(\mathbf{k})\rangle$ . Then  $E \rightarrow B$  becomes a *real* vector bundle. To preserve the reality condition, from now on we consider only  $\mathbf{O}(n)$  gauge transformations. As a consequence, the connection 1-form and the curvature 2-form take values in the orthogonal Lie group,  $\mathfrak{so}(n)$ . As these correspond to skew-symmetric matrices, the components of both of

these objects are skew-symmetric in band indices. In particular, this implies that the trace  $\mathbf{F} = -i \text{tr} \mathcal{F} = 0$ , i.e. Berry curvature of a real Hamiltonian vanishes whenever well-defined. The “well-defined” condition fails only when the matrix of states  $\mathcal{U}$  is not a differentiable function of  $\mathbf{k}$ , i.e. at band nodes. Indeed, band nodes of real Hamiltonians are known to carry a singular  $\pi$ -flux of the curvature.

While the change of Lie algebra  $\mathfrak{u}(n) \rightarrow \mathfrak{so}(n)$  trivializes Berry curvature, it also enables *new* gauge-invariant and topological objects. Decomposing into the basis of 1-forms,  $\mathcal{A} = \mathcal{A}_i dk^i$ , the prefactors  $\mathcal{A}_i$  are just skew-symmetric matrices. If we limit our attention to the case of an *even* number  $n$  of bands, then we can define *Euler connection*

$$\mathbf{a} = \text{Pf}(\mathcal{A}_i) dk^i \quad (19)$$

where Pf denotes Pfaffian. Below, we express the construction in Eq. (19) simply as “ $\mathbf{a} = \text{Pf}(\mathcal{A})$ ”. Gauge transformation of the Euler connection [i.e. combining Eq. (19) and Eq. (14) with  $X \in \mathbf{O}(n)$ ] for a general number of bands is a non-trivial task. However, for  $n = 2$  bands, the Pfaffian is a linear function of the matrix entries, therefore we can split

$$\begin{aligned} \tilde{\mathbf{a}} &= \text{Pf}(X^\top \mathcal{A} X) + \text{Pf}(X^\top dX) \\ &= \det(X) \mathbf{a} + \text{Pf}(X^\top dX) \quad (\text{for } n = 2 \text{ bands}), \end{aligned} \quad (20)$$

where we used the well-known identity that for an anti-symmetric matrix  $\mathcal{M}$  and an arbitrary matrix  $X$ ,

$$\text{Pf}(X^\top \mathcal{M} X) = \det(X) \text{Pf}(\mathcal{M}). \quad (21)$$

The sign  $\det(X) = \pm 1$  in Eq. (20) conveys whether we perform a proper (orientation-preserving) or an improper (orientation-reversing) gauge transformation.

Note that the Euler connection is *not* a matrix anymore, i.e. it can be treated as an ordinary differential 1-form. In particular, one can study the exterior derivative  $da$ . For a general number of bands, commuting the exterior derivative with the Pfaffian operator in Eq. (19) is a difficult task. However, for  $n = 2$  bands, the linearity of the Pfaffian implies that  $[d, \text{Pf}] = 0$ . We thus define

$$\text{Eu} := da \quad (\text{for } n = 2 \text{ bands}), \quad (22)$$

which is called the *Euler curvature* or *Euler form*. With a bit of manipulation, we obtain

$$\begin{aligned} \text{Eu} &= \text{Pf}(d\mathcal{A}) = \text{Pf}(\mathcal{F} - \underbrace{\mathcal{A} \wedge \mathcal{A}}_{=0}) \\ &= \text{Pf}(\mathcal{F}) \quad (\text{for } n = 2 \text{ bands}), \end{aligned} \quad (23)$$

where we used that  $(\mathcal{A} \wedge \mathcal{A})_{ij} = A_i A_j - A_j A_i = 0$  for  $\mathfrak{so}(2)$  matrices due to commutativity of their product. However, owing to the skew-symmetry of  $\mathcal{F}$ , the last line of Eq. (23) makes sense for *arbitrary* even  $n$ . We therefore lift this equation to be the *definition* of the Euler form

for an arbitrarily large collection of real bands,

$$\text{Eu} := \text{Pf}(\mathcal{F}_{ij}) dk^i \wedge dk^j. \quad (\text{for arbitrary } n), \quad (24)$$

Combining Eqs. (17) and (21), we find that under gauge transformations,

$$\tilde{\text{Eu}} = \det(X) \text{Eu}, \quad (25)$$

meaning that the Euler form is invariant under orientation-preserving  $\text{SO}(n)$  transformations of the  $n$  bands, while it flips sign under orientation-reversing transformations.

### 3. Quantization of Euler class

If the rank of the bundle is  $n = 2$ , and the base space is two-dimensional and parameterized by momenta  $k_x$  and  $k_y$ , then the Euler curvature

$$\text{Eu} = (\langle \partial_{k_x} u^1 | \partial_{k_y} u^2 \rangle - \langle \partial_{k_y} u^1 | \partial_{k_x} u^2 \rangle) dk^x \wedge dk^y, \quad (26)$$

is a single-component object. If further both the base space and the vector bundle are *orientable*, the Euler curvature can be treated as a volume form, and integrated over the base space  $B$ . Note that the nilpotence  $d^2 = 0$  implies that the exterior derivative of the Euler curvature is zero. However, the potential may not be globally defined, therefore the Euler class of an oriented real bundle on a base space  $B$  defines an element of the de Rham cohomology  $H_{\text{dR}}^2(B)$ . In fact, it can be shown [40] that  $\frac{1}{2\pi} \text{Eu}(\mathbf{k})$  integrates to an *integer* if the base space does not have a boundary, therefore the Euler form defines an element of the singular cohomology with *integer* coefficients,  $H^2(B; \mathbb{Z})$  [66]. The integer

$$\chi(E) = \frac{1}{2\pi} \oint_B \text{Eu} \quad (\text{for } n = 2 \text{ bands}) \quad (27)$$

is called the *Euler class* of the vector bundle  $E$ . The name is motivated by the observation that for a tangent bundle  $TM$  of a two-dimensional manifold  $M$  without a boundary, the integer  $\chi(TM)$  reproduces the *Euler characteristic* of  $M$  [65]. This observation for  $n = 2$  is a special case of the more general Chern-Gauss-Bonnet theorem [67], which applies to manifolds without boundary of higher even dimensions. Note also that the Euler characteristic of any odd-dimensional closed manifold is zero [68], thus justifying our motivation to consider real Hamiltonians with *even* number  $n$  of bands.

We remark that Eq. (27) is analogous to the definition of the first Chern number

$$c_1(E) = \frac{1}{2\pi} \oint_B \mathbf{F} \quad (28)$$

which is an element of  $H^2(B; \mathbb{Z})$  for *complex* vector bundles. The mathematical arguments guaranteeing the

quantization of  $\chi(E)$  resp.  $c_1(E)$  are essentially identical [66], and based on considering a covering of the base space  $B$  with open discs  $\{\mathcal{D}_\alpha\}_{\alpha=1}^N$ . To outline the argument, let us explicitly consider the case of  $B$  being a 2-sphere ( $S^2$ ). The sphere is covered by  $N = 2$  discs, e.g. the northern hemisphere  $\mathcal{D}_{\text{north}}$  and the southern hemisphere  $\mathcal{D}_{\text{south}}$ , which meet at the equator  $\gamma_{\text{eq.}}$ . Since disc is a contractible manifold, we can use Stokes' theorem to relate  $\int_{\mathcal{D}_\alpha} \text{Eu}$  to  $\oint_{\partial \mathcal{D}_\alpha} a$  (and analogously  $\int_{\mathcal{D}_\alpha} \mathbf{F}$  to  $\oint_{\partial \mathcal{D}_\alpha} A$  for the complex case) on each hemisphere. The resulting two integrals run around the equator in opposite directions, therefore

$$\begin{aligned} 2\pi\chi(E) &= \oint_{S^2} \text{Eu} = \int_{\mathcal{D}_{\text{north}}} \text{Eu} + \int_{\mathcal{D}_{\text{south}}} \text{Eu} \\ &= \oint_{\gamma_{\text{eq.}}} (a_{\text{north}} - a_{\text{south}}) \\ &= \oint_{\gamma_{\text{eq.}}} \text{Pf}[X^\top dX] \quad (\text{for } n = 2 \text{ bands}) \end{aligned} \quad (29)$$

where in the last expression we used that the connections  $a_{\text{north}}$  and  $a_{\text{south}}$  on the two hemispheres for rank-2 bundles are related by a gauge transformation in Eq. (20), and we assumed that the orientation of the vector bundle is fixed on the whole 2-sphere [thus  $\det(X) = +1$ ]. Note that if we write the  $\text{SO}(2)$  matrix  $X$  using the algebra element  $\alpha \in \mathfrak{so}(2)$  as  $X = e^{+i\alpha\sigma_y}$ , then the last expression in Eq. (29) reduces to integration of  $\text{Pf}[X^\top dX] = d\alpha$ . Since the gauge transformation  $X$  must return to its original form after traversing the equator, the value of  $\alpha$  must increase by an integer multiple of  $2\pi$  on  $\gamma_{\text{eq.}}$ . Therefore

$$2\pi\chi(E) = \oint_{\gamma_{\text{eq.}}} d\alpha = 2\pi m \quad (30)$$

$$\text{with } m \in \mathbb{Z} \quad (\text{for } n = 2 \text{ bands}) \quad (31)$$

which completes the proof of the quantization of the Euler class for real orientable rank-2 vector bundles on  $S^2$ .

### 4. Complexification of rank-2 real vector bundle

We finally comment on the correspondence between the Euler form of two real states  $|u^{1,2}\rangle$  and the Berry curvature of the complex state  $|\psi\rangle = \frac{1}{\sqrt{2}}(|u^1\rangle + i|u^2\rangle)$ , which we briefly mention in the main text. A simple calculation for the single-band Berry curvature according to Eq. (18) first reveals that

$$\mathbf{F}_{ij} = -i \langle \partial_{k_i} \psi | \partial_{k_j} \psi \rangle + \text{c.c.} \quad (32)$$

$$\begin{aligned} &= -\frac{i}{2} \left( \langle \partial_{k_i} u^1 | \partial_{k_j} u^1 \rangle + \langle \partial_{k_i} u^2 | \partial_{k_j} u^2 \rangle \right. \\ &\quad \left. + i \langle \partial_{k_i} u^1 | \partial_{k_j} u^2 \rangle - i \langle \partial_{k_i} u^2 | \partial_{k_j} u^1 \rangle \right) + \text{c.c.} \end{aligned} \quad (33)$$

where c.c. stands for “complex conjugate”. Due to reality condition on the states  $|u^{1,2}\rangle$ , the expressions



$-i\langle\partial_{k_i}u^a|\partial_{k_j}u^a\rangle$  for  $a = 1, 2$  are purely imaginary, meaning that they drop under the combination with the c.c. part. In contrast, the two terms in the second line of Eq. (33) are real, therefore combination with c.c. leads to doubling, and we find

$$F_{ij} = \langle\partial_{k_i}u^1|\partial_{k_j}u^2\rangle - \langle\partial_{k_i}u^2|\partial_{k_j}u^1\rangle + \text{c.c.} = \text{Eu}_{ij} \quad (34)$$

where we recognized the componentwise version of Eq. (26). The identification

$$\text{Eu}\left[|u^1\rangle, |u^2\rangle\right] = F\left[\frac{1}{\sqrt{2}}(|u^1\rangle + i|u^2\rangle)\right] \quad (35)$$

allows us to numerically compute Euler form with the help of various tricks known from the numerical computation of Berry curvature, such as the projection onto the complex state along an infinitesimal square path, cf. Ref. [69]. We comment on the relation in Eq. (35) again in Sec. H when outlining our numerical algorithm. We emphasize that Eq. (35) is true for a pair of bands in models of arbitrarily high rank.

#### D. Euler form in three-band models

In this section, we further elaborate on the analogy between the Euler class and the first Chern number by briefly focusing on the minimal models. More specifically, we show that both the Berry curvature  $F(\mathbf{k})$  of one band obtained from a two-band complex Hamiltonian, as well as the Euler form  $\text{Eu}(\mathbf{k})$  of two bands obtained from a three-band real Hamiltonian, can be understood by considering geometry on a 2-sphere ( $S^2$ ). The discussion below thus proves the geometric interpretation of Euler form presented in Fig. 4(b) of the main text. We note that this section provides a slight digression from the theoretical notions presented in previous sections and we return to the general case of real models with an arbitrary number of bands.

Let us first recall the mathematics behind the first Chern number of a complex Hamiltonian, defined in Eq. (28), for the case of two bands. Hermitian two-band Hamiltonians can be decomposed using the Pauli matrices and the unit matrix as

$$H(\mathbf{k}) = \mathbf{h}(\mathbf{k}) \cdot \boldsymbol{\sigma} + h_0(\mathbf{k})\mathbb{1} \quad (36)$$

where  $h_{0,x,y,z}(\mathbf{k})$  are real functions of momentum. Spectral flattening brings eigenvalues of the Hamiltonian to  $\pm 1$  without changing the band topology [6], and is associated with replacing  $h_0 \mapsto 0$  and  $\mathbf{h} \mapsto \mathbf{h}/\|\mathbf{h}\| \equiv \mathbf{n}$ . The band topology of the two-band complex Hamiltonian is thus completely captured by the three-component unit vector  $\mathbf{n}(\mathbf{k}) \in S^2$ . It is known [2, 3] that the Berry curvature of one of the two bands can be expressed as

$$F_{ij} = \frac{1}{2}\mathbf{n} \cdot (\partial_{k_i}\mathbf{n} \times \partial_{k_j}\mathbf{n}), \quad (37)$$

such that  $F_{ij} dk_i dk_j$  corresponds to one half of the (oriented) solid angle spanned by  $\mathbf{n}$  on the  $S^2$  as the momentum argument is varied over a rectangle of size  $dk_i \times dk_j$ . For a *closed* two-dimensional base manifold, the vector  $\mathbf{n}$  has to wrap around the unit sphere an integer number of times, hence the integral of  $F_{ij} dk_i dk_j$ , i.e. the total (oriented) solid angle spanned by  $\mathbf{n}$ , must be quantized to integer multiples of  $2\pi$ . Therefore,  $c_1(E)$  defined in Eq. (28) is an integer. This simple argument does not generalize to models with more than two bands, in which case one has to follow the proof outlined at the end of Sec. C.

We find that a very similar geometric interpretation also applies to Euler form of two bands obtained from a three-band real Hamiltonian. In this case, spectral flattening brings the Hamiltonian with two occupied bands and one unoccupied band to [39]

$$H(\mathbf{k}) = 2\mathbf{n}(\mathbf{k}) \cdot \mathbf{n}(\mathbf{k})^\top - \mathbb{1}, \quad (38)$$

where  $\mathbf{n}(\mathbf{k}) = \mathbf{u}^1(\mathbf{k}) \times \mathbf{u}^2(\mathbf{k}) \in S^2$  is the (normalized) column vector representing the unoccupied state, which can be represented as cross product of the (normalized) occupied states  $\mathbf{u}^1(\mathbf{k})$  and  $\mathbf{u}^2(\mathbf{k})$ . Note that, because of the reality condition, the left (“bra”) and the right (“ket”) eigenstates are componentwise equal to each other. The quadratic dependence of the Hamiltonian on the unit vector, manifest in Eq. (38), implies that vectors  $\pm\mathbf{n}$  represent the same Hamiltonian. Therefore the space of *unique* spectrally flattened 3-band Hamiltonians is  $S^2/\mathbb{Z}_2 \equiv \mathbb{RP}^2$  [25]. However, if the vector bundle defined by  $H(\mathbf{k})$  is orientable (which is a necessary condition to define Euler form), then there are no closed paths  $\gamma \subset B$  in the base manifold which would be mapped by the Hamiltonian to the non-contractible path in  $\mathbb{RP}^2$ . Therefore, Euler form of an *orientable* rank-2 bundle obtained from a three-band real Hamiltonian, is related to geometry on  $S^2$ . In fact, we show below that

$$\text{Eu}_{ij} = \mathbf{n} \cdot (\partial_{k_i}\mathbf{n} \times \partial_{k_j}\mathbf{n}), \quad (39)$$

which [besides the altered interpretation of  $\mathbf{n}(\mathbf{k})$ ] qualitatively differs from Eq. (37) only in the absence of the prefactor  $\frac{1}{2}$ . Following the same arguments as for the first Chern number, we find that for three-band models the Euler class  $\chi(E)$  defined in Eq. (27) must be an *even* integer. This agrees with the known fact, that odd values of the Euler class (corresponding to a non-trivial second Stiefel-Whitney class) require models with at least two occupied and with at least two unoccupied bands [31]. We also remark that the cross-product definition of  $\mathbf{n}(\mathbf{k})$  in terms of the two occupied states makes the expression in Eq. (39) invariant only under the *proper*  $\text{SO}(2)$  gauge transformations of the occupied states, reminding us of the importance of orientability of the vector bundle.

The remainder of this section contains a proof of Eq. (39). While the logic of the proof is straightforward, some of the expressions are rather lengthy. We employ

the Einstein summation convention, and we write

$$n_a = \epsilon_{abc} u_b^1 u_c^2 \quad (40)$$

where  $\epsilon$  is the Levi-Civita symbol. The right-hand side

of Eq. (39) can be expressed as

$$(39) = \epsilon_{abc} u_b^1 u_c^2 \epsilon_{ade} \partial_{k_i} (\epsilon_{dfg} u_f^1 u_g^2) \partial_{k_j} (\epsilon_{ehi} u_h^1 u_i^2). \quad (41)$$

Using the identity  $\epsilon_{abc} \epsilon_{ade} = \delta_{bd} \delta_{ce} - \delta_{be} \delta_{cd}$ , and performing the summation over indices  $b$  and  $c$ , we obtain

$$(39) = \epsilon_{dfg} \epsilon_{ehi} (u_d^1 u_e^2 - u_e^1 u_d^2) \partial_{k_i} (u_f^1 u_g^2) \partial_{k_j} (u_h^1 u_i^2). \quad (42)$$

To get rid off the remaining Levi-Civita symbols, we use

$$\epsilon_{dfg} \epsilon_{ehi} = \delta_{de} (\delta_{fh} \delta_{gi} - \delta_{fi} \delta_{gh}) - \delta_{dh} (\delta_{fe} \delta_{gi} - \delta_{fi} \delta_{ge}) + \delta_{di} (\delta_{fe} \delta_{gh} - \delta_{fh} \delta_{ge}). \quad (43)$$

This long identity has to be substituted into Eq. (42). Note that the combinations of Kronecker symbols containing  $\delta_{de}$  trivially lead to zero after the substitution, because  $\delta_{de} (u_d^1 u_e^2 - u_e^1 u_d^2) = 0$ . The remaining terms in Eq. (43), after summing over indices  $e$ ,  $h$ , and  $i$ , lead to

$$(39) = -(u_d^1 u_f^2 - u_f^1 u_d^2) \partial_{k_i} (u_f^1 u_g^2) \partial_{k_j} (u_d^1 u_g^2) + (u_d^1 u_g^2 - u_g^1 u_d^2) \partial_{k_i} (u_f^1 u_g^2) \partial_{k_j} (u_d^1 u_f^2) \\ + (u_d^1 u_f^2 - u_f^1 u_d^2) \partial_{k_i} (u_f^1 u_g^2) \partial_{k_j} (u_g^1 u_d^2) - (u_d^1 u_g^2 - u_g^1 u_d^2) \partial_{k_i} (u_f^1 u_g^2) \partial_{k_j} (u_f^1 u_g^2) \quad (44)$$

Performing the derivatives by parts, Eq. (44) expands into 32 individual terms

$$(39) = -u_d^1 u_f^2 (\partial_{k_i} u_f^1) u_g^2 (\partial_{k_j} u_d^1) u_g^2 - u_d^1 u_f^2 (\partial_{k_i} u_f^1) u_g^2 u_d^1 (\partial_{k_j} u_g^2) - u_d^1 u_f^2 u_f^1 (\partial_{k_i} u_g^2) (\partial_{k_j} u_d^1) u_g^2 - u_d^1 u_f^2 u_f^1 (\partial_{k_i} u_g^2) u_d^1 (\partial_{k_j} u_g^2) \\ + u_f^1 u_d^2 (\partial_{k_i} u_f^1) u_g^2 (\partial_{k_j} u_d^1) u_g^2 + u_f^1 u_d^2 (\partial_{k_i} u_f^1) u_g^2 u_d^1 (\partial_{k_j} u_g^2) + u_f^1 u_d^2 u_f^1 (\partial_{k_i} u_g^2) (\partial_{k_j} u_d^1) u_g^2 + u_f^1 u_d^2 u_f^1 (\partial_{k_i} u_g^2) u_d^1 (\partial_{k_j} u_g^2) \\ + u_d^1 u_g^2 (\partial_{k_i} u_f^1) u_g^2 (\partial_{k_j} u_d^1) u_f^2 + u_d^1 u_g^2 (\partial_{k_i} u_f^1) u_g^2 u_d^1 (\partial_{k_j} u_f^2) + u_d^1 u_g^2 u_f^1 (\partial_{k_i} u_g^2) (\partial_{k_j} u_d^1) u_f^2 + u_d^1 u_g^2 u_f^1 (\partial_{k_i} u_g^2) u_d^1 (\partial_{k_j} u_f^2) \\ - u_g^1 u_d^2 (\partial_{k_i} u_f^1) u_g^2 (\partial_{k_j} u_d^1) u_f^2 - u_g^1 u_d^2 (\partial_{k_i} u_f^1) u_g^2 u_d^1 (\partial_{k_j} u_f^2) - u_g^1 u_d^2 u_f^1 (\partial_{k_i} u_g^2) (\partial_{k_j} u_d^1) u_f^2 - u_g^1 u_d^2 u_f^1 (\partial_{k_i} u_g^2) u_d^1 (\partial_{k_j} u_f^2) \\ + u_d^1 u_f^2 (\partial_{k_i} u_f^1) u_g^2 (\partial_{k_j} u_d^1) u_d^2 + u_d^1 u_f^2 (\partial_{k_i} u_f^1) u_g^2 u_d^1 (\partial_{k_j} u_d^2) + u_d^1 u_f^2 u_f^1 (\partial_{k_i} u_g^2) (\partial_{k_j} u_d^1) u_d^2 + u_d^1 u_f^2 u_f^1 (\partial_{k_i} u_g^2) u_d^1 (\partial_{k_j} u_d^2) \\ - u_f^1 u_d^2 (\partial_{k_i} u_f^1) u_g^2 (\partial_{k_j} u_d^1) u_d^2 - u_f^1 u_d^2 (\partial_{k_i} u_f^1) u_g^2 u_d^1 (\partial_{k_j} u_d^2) - u_f^1 u_d^2 u_f^1 (\partial_{k_i} u_g^2) (\partial_{k_j} u_d^1) u_d^2 - u_f^1 u_d^2 u_f^1 (\partial_{k_i} u_g^2) u_d^1 (\partial_{k_j} u_d^2) \\ - u_d^1 u_g^2 (\partial_{k_i} u_f^1) u_g^2 (\partial_{k_j} u_f^1) u_d^2 - u_d^1 u_g^2 (\partial_{k_i} u_f^1) u_g^2 u_d^1 (\partial_{k_j} u_f^2) - u_d^1 u_g^2 u_f^1 (\partial_{k_i} u_g^2) (\partial_{k_j} u_f^1) u_d^2 - u_d^1 u_g^2 u_f^1 (\partial_{k_i} u_g^2) u_d^1 (\partial_{k_j} u_f^2) \\ + u_g^1 u_d^2 (\partial_{k_i} u_f^1) u_g^2 (\partial_{k_j} u_f^1) u_d^2 + u_g^1 u_d^2 (\partial_{k_i} u_f^1) u_g^2 u_d^1 (\partial_{k_j} u_f^2) + u_g^1 u_d^2 u_f^1 (\partial_{k_i} u_g^2) (\partial_{k_j} u_f^1) u_d^2 + u_g^1 u_d^2 u_f^1 (\partial_{k_i} u_g^2) u_d^1 (\partial_{k_j} u_f^2)$$

Most of these 32 terms vanish. To see this, we use orthonormality  $u_a^1 u_a^2 = 0$  on the vector coordinates displayed in **red**. Furthermore, the normalization  $u_a^1 u_a^1 = 1 = u_a^2 u_a^2$  implies that  $u_a^1 (\partial_{k_\beta} u_a^1) = 0 = u_a^2 (\partial_{k_\beta} u_a^2)$ , which we indicate in **blue**. Only two terms remain, in which we further use the normalization to 1 on vector components displayed in **green**. After renaming the repeated indices, we obtain

$$\text{Eu}_{ij} = (\partial_{k_i} u_f^1) (\partial_{k_j} u_f^2) - (\partial_{k_j} u_f^1) (\partial_{k_i} u_f^2) \equiv \langle \partial_{k_i} u^1 | \partial_{k_j} u^2 \rangle - \langle \partial_{k_j} u^1 | \partial_{k_i} u^2 \rangle. \quad (45)$$

The last expression exactly corresponds to the components of the the Euler form over two bands as defined in Eq. (26). This completes the proof of Eq. (39).

## E. Analytic properties of Euler form at principal nodes

### 1. General remarks

In the main text we consider the Euler form  $\text{Eu}(\mathbf{k})$  defined by the two principal bands. Note that adjacent nodes pose problems for the mathematical construction. This is because circumnavigating an adjacent node reverses the orientation of one of the principal Bloch states (the one that participates in the formation of the node), but not the other one. Therefore, parallel transport around an adjacent node is associated with an *improper*

gauge transformation  $X = \sigma_z \notin \text{SO}(2)$ . Since such vector bundle is not orientable, its Euler curvature cannot be defined. This is the reason why we only consider calculations over regions with no adjacent nodes.

On the other hand, the behavior of the Euler form near a *principal* node is more subtle. First, circumnavigating a principal node reverses the sign of *both* principal Bloch states, which corresponds to a *proper* gauge transformation  $X = -\mathbb{1} \in \text{SO}(2)$ , such that Euler form of the bundle is well-defined on an annulus around the node. On the other hand, the eigenstates of the Hamiltonian are not continuous functions of  $\mathbf{k}$  at the location of principal nodes, suggesting that the derivatives of the

eigenstates are not well-defined at these points. Nevertheless, the rank-2 vector bundle spanned by the two principal bands is actually continuous and differentiable at principal nodes. The last two statements are not in contradiction! Indeed, a discontinuous basis of the bundle does not imply discontinuity of the bundle. There may be (and we show that there really is) a different basis which is perfectly continuous at principal nodes.

However, one has to consider the relevance of the two bases for physical observables. Since the two principal bands are separated by a band gap away from the principal nodes, the discontinuous basis of the bundle corresponding to the principal eigenstates has a *special physical significance*. Especially, we show in Sec. F that this canonical (although discontinuous) basis encodes observable features, such as the path-dependent ability of band nodes to annihilate. This information is lost once we allow for mixing of the two principal eigenstates by a general  $\text{SO}(2)$  gauge transformation – such as when going to the basis that reveals the continuity of the bundle.

The physical importance of the eigenstate basis can be naturally built into the mathematical description by introducing the notion of a *flag bundle* [70], and by contrasting it to the more familiar notion of a *vector bundle*. On the one hand, the two principal bands span a two-dimensional vector space that varies continuously as a function of  $\mathbf{k}$ . In other words, the two principal bands constitute a rank-two *vector bundle*. In this description, the two-dimensional vector space admits arbitrary  $\text{SO}(2)$  gauge transformations, and the physical eigenstate basis is not treated as being special. Therefore, in this description it is natural to adopt the continuous basis, where there are no singularities – and thus also no topological information. This is compatible with the well-known fact that any smooth vector bundle is trivializable over a patch (disk).

In contrast, a *flag bundle* keeps information about the subdivision of the two-dimensional vector space into two one-dimensional vector spaces, and thus preserves information about the two physical eigenstates. In this language, the admissible (orientation-preserving) gauge transformations of the two dimensional vector space are just  $\text{S}[\text{O}(1) \times \text{O}(1)] \cong \mathbb{Z}_2$  (corresponding to  $X = \pm \mathbb{1}$ , excluding  $X = \pm \sigma_z$ ). The flag bundle exhibits a singularity at the principal node, which is unremovable by admissible gauge transformations, and which can be described using a topological invariant – the Euler class. Note that the rank-2 flag bundle exhibits a singularity and topological invariant on a patch (disk), even though the corresponding rank-2 vector bundle is continuous and trivializable on the patch. This is because the vector bundle description carries less information, which is insufficient to describe the principal nodes.

In the remainder of this text, we avoid the notion of flag bundle. Instead, we speak of the *computation in the eigenstate basis*, which (based on the remark in the previous paragraphs) we except to convey topological information. This is contrasted to the *computation in the*

*continuous* (or *rotated*) basis, where no topological information is expected. However, the robustness of the invariant derived in the eigenstates basis cannot be rigorously justified within the vector bundle description, and only comes from the restricted  $\text{S}[\text{O}(1) \times \text{O}(1)] \cong \mathbb{Z}_2$  gauge transformation of the flag bundle formalism.

## 2. Computation in the eigenstate basis

We begin our discussion by presenting the most general Hamiltonian near a principal node to the linear order in momentum. We treat the obtained Hamiltonian perturbatively, and we consider the *eigenstate basis* to reveal the structure of the Euler form near the principal node.

We first consider a two-band model that exhibits a node at  $\mathbf{k} = \mathbf{0}$  at zero energy. To linear order, the Hamiltonian near the node must take the form

$$\mathcal{H}_{2\text{-band}}(\mathbf{k}) = \sum_{i=1}^2 \sum_{j=0}^3 k_i h_{ij} \sigma_j \quad (46)$$

where  $k_{1,2}$  are the two momentum coordinates,  $h_{ij}$  are 8 real coefficients, and  $\{\sigma_j\}_{j=0}^3$  is the unit matrix and the three Pauli matrices. It is known that by a suitable proper rotation and by a linear rescaling of the momentum coordinates to  $\boldsymbol{\kappa}(\mathbf{k})$ , we can bring the Hamiltonian to the form

$$\mathcal{H}_{2\text{-band}}(\boldsymbol{\kappa}) = \begin{pmatrix} \kappa_1 + \varepsilon(\boldsymbol{\kappa}) & \pm \kappa_2 \\ \pm \kappa_2 & -\kappa_1 + \varepsilon(\boldsymbol{\kappa}) \end{pmatrix}, \quad (47)$$

where  $\varepsilon(\boldsymbol{\kappa}) = v_1 \kappa_1 + v_2 \kappa_2$  describes the tilting of the band node [43]. Since the considered coordinate transformation is linear, the associated Jacobian  $J_{ij} = \partial \kappa_i / \partial k_j$  is a constant matrix. The  $\pm$  sign corresponds to nodes with positive vs. negative winding number  $w \in \pi_1[\text{SO}(2)] = \mathbb{Z}$ , which we keep unspecified throughout the whole section.

If there are additional bands, then the same rotation of the two basis vectors brings the corresponding  $n$ -band linear-order Hamiltonian to the form

$$\mathcal{H}_{n\text{-band}}(\boldsymbol{\kappa}) = \begin{pmatrix} \kappa_1 + \varepsilon(\boldsymbol{\kappa}) & \pm \kappa_2 & f^\top(\boldsymbol{\kappa}) \\ \pm \kappa_2 & -\kappa_1 + \varepsilon(\boldsymbol{\kappa}) & g^\top(\boldsymbol{\kappa}) \\ f(\boldsymbol{\kappa}) & g(\boldsymbol{\kappa}) & \mathcal{E} + h(\boldsymbol{\kappa}) \end{pmatrix}, \quad (48)$$

where  $f(\boldsymbol{\kappa})$  and  $g(\boldsymbol{\kappa})$  are  $\boldsymbol{\kappa}$ -linear  $(n-2)$ -component column vectors with real components  $\{f_c(\boldsymbol{\kappa})\}_{c=3}^n$  and  $\{g_c(\boldsymbol{\kappa})\}_{c=3}^n$ ,  $\mathcal{E}$  is a non-degenerate diagonal matrix of  $(n-2)$  non-zero band energies, and  $h(\boldsymbol{\kappa})$  is  $\boldsymbol{\kappa}$ -linear Hermitian matrix of size  $(n-2) \times (n-2)$ . In Eq. (48) we explicitly assume that the additional  $(n-2)$  basis vectors of the Hilbert space are given by the additional eigenstates of the Hamiltonian at the node, therefore  $h(\boldsymbol{\kappa} = \mathbf{0}) = \mathbb{0}$ . Therefore, after adopting the properly rotated and rescaled momentum coordinates and the right Hilbert-space basis, the model in Eq. (48) represents the *most general  $n$ -band real Hamiltonian near a principal*

node to linear order in momentum.

To proceed, we split the Hamiltonian in Eq. (48) into  $\mathcal{H}_0 = \text{diag}(\epsilon(\boldsymbol{\kappa}), \epsilon(\boldsymbol{\kappa}), \mathcal{E})$ , and a “perturbation”  $\mathcal{H}'$  that contains all the terms linear in  $\boldsymbol{\kappa}$ , that is

$$\mathcal{H}'(\boldsymbol{\kappa}) = \begin{pmatrix} \kappa_1 & \pm\kappa_2 & f^\top(\boldsymbol{\kappa}) \\ \pm\kappa_2 & -\kappa_1 & g^\top(\boldsymbol{\kappa}) \\ f(\boldsymbol{\kappa}) & g(\boldsymbol{\kappa}) & h(\boldsymbol{\kappa}) \end{pmatrix}. \quad (49)$$

The first step of the perturbation theory requires us to find states that diagonalize the matrix  $\mathcal{H}'_{ab} = \langle a | \mathcal{H}' | b \rangle$  with  $a, b \in \{1, 2\}$  representing the degenerate states at the principal nodes. We take  $|1\rangle = (1 \ 0 \ 0 \ \dots)^\top$  and  $|2\rangle = (0 \ 1 \ 0 \ \dots)^\top$ , in which case this matrix corresponds simply to the upper-left  $2 \times 2$  block of Eq. (49). If we further decompose  $\boldsymbol{\kappa}$  using the polar coordinates as  $\kappa_1 = \kappa \cos \phi$  and  $\kappa_2 = \kappa \sin \phi$ , this block is diagonalized by

$$|1^{(0)}\rangle = \begin{pmatrix} \pm \sin \frac{\phi}{2} \\ -\cos \frac{\phi}{2} \\ \mathbf{0} \end{pmatrix} \quad \text{and} \quad |2^{(0)}\rangle = \zeta \begin{pmatrix} +\cos \frac{\phi}{2} \\ \pm \sin \frac{\phi}{2} \\ \mathbf{0} \end{pmatrix} \quad (50)$$

where  $\zeta = \pm 1$  corresponds to two different orientations of the bundle. Changing the relative sign between the two states corresponds to orientation-changing gauge transformation  $X = \pm \sigma_z$ . On the other hand, increasing  $\phi \mapsto \phi + 2\pi$  flips the sign of *both* bands, which corresponds to a proper gauge transformation  $X = -1$ .

The first-order correction to the states in Eq. (50) is given by

$$|a^{(1)}\rangle = \sum_{c=3}^n \frac{\langle c | \mathcal{H}' | a^{(0)} \rangle}{\epsilon(\boldsymbol{\kappa}) - \mathcal{E}_c} |c\rangle \quad (51)$$

where  $|c\rangle$  is the  $c^{\text{th}}$  element of the basis in which we expressed Eq. (49). This prescription does not lead to a change in the first two components of the principal vectors, while for components with  $c \geq 3$  we find

$$\langle c | 1^{(1)} \rangle = \frac{1}{\epsilon(\boldsymbol{\kappa}) - \mathcal{E}_c} \left[ \pm f_c(\boldsymbol{\kappa}) \sin \frac{\phi}{2} - g_c(\boldsymbol{\kappa}) \cos \frac{\phi}{2} \right] \quad (52)$$

$$\langle c | 2^{(1)} \rangle = \frac{\zeta}{\epsilon(\boldsymbol{\kappa}) - \mathcal{E}_c} \left[ +f_c(\boldsymbol{\kappa}) \cos \frac{\phi}{2} \pm g_c(\boldsymbol{\kappa}) \sin \frac{\phi}{2} \right]. \quad (53)$$

Note that the expressions inside the square brackets are linear in  $\boldsymbol{\kappa}$ , while the prefactor can be approximated for  $\boldsymbol{\kappa}$  close to  $\mathbf{0}$  as

$$\frac{1}{\epsilon(\boldsymbol{\kappa}) - \mathcal{E}_c} \approx -\frac{1}{\mathcal{E}_c} + \frac{v_1 \kappa_1 + v_2 \kappa_2}{\mathcal{E}_c^2}. \quad (54)$$

Therefore, if we are after terms of the lowest order in  $\boldsymbol{\kappa}$ , we can approximate the prefactor simply by  $-1/\mathcal{E}_c$ . Furthermore, notice that states  $|1^{(0+1)}\rangle$  and  $|2^{(0+1)}\rangle$ , which we obtained by performing the first-order perturbation theory, are not properly normalized. However, since the lowest-order corrections  $|1^{(1)}\rangle$  and  $|2^{(1)}\rangle$  are *linear* in  $\boldsymbol{\kappa}$ , the correction from the proper normalization would be *quadratic* in  $\boldsymbol{\kappa}$ . More explicitly, normalizing the states

would induce a prefactor of the form

$$\frac{1}{\sqrt{1 + \|\boldsymbol{\kappa}\mathcal{N}\|^2}} \approx 1 - \frac{1}{2} \|\boldsymbol{\kappa}\mathcal{N}\|^2 \quad (55)$$

where  $\|\boldsymbol{\kappa}\mathcal{N}\|$  represents the normalization of the first-order correction. Since we are interested only in corrections to the principal states of the *lowest order* in  $\boldsymbol{\kappa}$ , we safely ignore the normalization.

We have established the lowest-order (linear) corrections in  $\boldsymbol{\kappa}$  to the principal Bloch states in Eq. (50). We can use the obtained states to calculate the Euler connection and the Euler form *in the eigenstate basis*,

$$a_i = \langle 1 | \partial_{\kappa_i} 2 \rangle \quad \text{and} \quad \text{Eu} = \langle \partial_{\kappa_1} 1 | \partial_{\kappa_2} 2 \rangle - \langle \partial_{\kappa_2} 1 | \partial_{\kappa_1} 2 \rangle \quad (56)$$

where we dropped the superscript “(0+1)” for brevity. However, note that the symbolic computation of the derivatives in Eq. (56) cannot be fully trusted for  $k \rightarrow 0$  because of the discontinuity of the states in Eq. (50) at  $k = 0$ . Nevertheless, for now we ignore this possible source of problem. To proceed, we use that

$$\partial_{\kappa_1} = \frac{\partial \kappa}{\partial \kappa_1} \partial_\kappa + \frac{\partial \phi}{\partial \kappa_1} \partial_\phi = \cos \phi \partial_\kappa - \frac{\sin \phi}{\kappa} \partial_\phi \quad (57)$$

$$\partial_{\kappa_2} = \frac{\partial \kappa}{\partial \kappa_2} \partial_\kappa + \frac{\partial \phi}{\partial \kappa_2} \partial_\phi = \sin \phi \partial_\kappa + \frac{\cos \phi}{\kappa} \partial_\phi. \quad (58)$$

We also rewrite

$$f_c(\boldsymbol{\kappa}) = \alpha_c \kappa \cos \phi + \beta_c \kappa \sin \phi \quad (59)$$

$$g_c(\boldsymbol{\kappa}) = \gamma_c \kappa \cos \phi + \delta_c \kappa \sin \phi. \quad (60)$$

With the help of **Mathematica**, we find the Euler connection to the leading order in  $\kappa$  as

$$\mathbf{a} = \frac{\pm \zeta}{2\kappa} (\sin \phi, -\cos \phi) + \mathcal{O}(\kappa) \quad (61)$$

which *diverges* as we approach the node. In contrast, the Euler form to the leading order in  $\kappa$  is

$$\begin{aligned} \text{Eu} = & -\zeta \sum_{c=3}^n \frac{1}{\mathcal{E}_c^2} \left[ (\beta_c \gamma_c - \alpha_c \delta_c) \right. \\ & \left. \pm \frac{1}{2} (\alpha_c \cos \phi + \beta_c \sin \phi)^2 \pm \frac{1}{2} (\gamma_c \cos \phi + \delta_c \sin \phi)^2 \right] \\ & (\text{wrong!} - \text{read end of Sec. E 2}) \end{aligned} \quad (62)$$

which *does not diverge* at the node. All the  $1/\kappa$  factors, present in some of the previous formulae, cancel out. Substituting back the original coordinates,  $\boldsymbol{\kappa} \rightarrow \mathbf{k}$ , corresponds to a double multiplication by the (constant) Jacobian matrix, which also does not induce a divergence. One is tempted to conclude that Eu is discontinuous at principal nodes, which prevents the applicability of Stokes’ theorem. On the other hand, the singularity in Eq. (62) is integrable, which suggests that the definition of Euler class in Eq. (5) of the main text is mathematically meaningful. By integrating over an infinitesimal disk  $\mathcal{D}^\epsilon$  with radius  $\epsilon$  around the principal node, we find



$\lim_{\epsilon \rightarrow 0} \int_{\mathcal{D}^\epsilon} \text{Eu} = 0$  and  $\lim_{\epsilon \rightarrow 0} \oint_{\partial \mathcal{D}^\epsilon} \mathbf{a} = \mp \pi \zeta$ , such that the Euler class on the disk [cf. Eq. (5) of the main text, and Sec. F below]

$$\chi(\mathcal{D}^\epsilon) = \mp \frac{\zeta}{2} \quad (63)$$

is non-zero, and carries topological information.

However, as we warned before Eq. (57), the *presented computation cannot be fully trusted due to the discontinuity of states  $|1\rangle$  and  $|2\rangle$  at  $\kappa = 0$* . This means that both the Euler connection and Euler form are, strictly speaking, undefined at  $\kappa = 0$ , and we have attempted to perform a series expansion around a singular point. It turns out that our result for Euler connection  $\mathbf{a}$  in Eq. (61) is correct. In contrast, as we convincingly show in the next subsection, the result for the Euler connection  $\text{Eu}$  in Eq. (62) is *wrong!* – namely the whole discontinuous contribution to  $\text{Eu}$  in the *second line of Eq. (62) should not be there*. The Euler form is therefore continuous at the principal node, and what really prevents the applicability of the Stokes' theorem is the divergence of  $\mathbf{a}$  for  $\kappa \rightarrow 0$  observed in Eq. (61).

### 3. Computation in the rotated (continuous) basis

In the previous subsection, we attempted to derive the analytic properties of Euler connection and Euler curvature by performing the computation in the eigenstate basis. However, the discontinuous nature of the eigenstates at the principal node led to some uncontrolled steps, and the derived results cannot be fully trusted. Here, we approach the problem differently. We perform a gauge transformation to a *rotated basis*, which reveals the continuity of the vector bundle spanned by the two principal bands and principal nodes. The continuity allows us to keep the computation of Euler form and Euler connection under control. At the end of the calculation, we perform a large gauge transformation back to eigenstate basis, and compare to the results obtained in Sec. E2. While this is admittedly a somewhat indirect approach to derive the results, the advantage is that we only have to deal with the singularity at the very last step when we do the gauge transformation back to the eigenstate basis.

Recall that a rank-2 bundle is a collection of two-dimensional planes – one plane per every point of the base space. The specific choice of these planes varies continuously between the points of the base space. Importantly, these planes need not in general be equipped with any intrinsic basis. The basis vectors that we use to span these planes are just an auxiliary tool. Performing an  $\text{SO}(2)$  gauge transformation on the two vectors spanning the rank-2 bundle does not correspond to a change of the bundle, just to a *change of coordinates* that we use to describe the bundle. In particular, it is convenient to

consider the “mixed” (i.e. *rotated*) states

$$|A(\boldsymbol{\kappa})\rangle = \pm \sin \frac{\phi}{2} |1^{(0+1)}\rangle + \zeta \cos \frac{\phi}{2} |2^{(0+1)}\rangle \quad (64)$$

$$|B(\boldsymbol{\kappa})\rangle = -\zeta \cos \frac{\phi}{2} |1^{(0+1)}\rangle \pm \sin \frac{\phi}{2} |2^{(0+1)}\rangle \quad (65)$$

which are related to the eigenstates of the perturbed Hamiltonian by a proper gauge transformation

$$X(\boldsymbol{\kappa}; \zeta) = \begin{pmatrix} \pm \sin \frac{\phi}{2} & +\zeta \cos \frac{\phi}{2} \\ -\zeta \cos \frac{\phi}{2} & \pm \sin \frac{\phi}{2} \end{pmatrix} \quad (66)$$

Using trigonometric identities, we find that to linear order in  $\boldsymbol{\kappa}$  these rotated vectors are

$$|A(\boldsymbol{\kappa})\rangle = \begin{pmatrix} 1 \\ 0 \\ \{-\frac{f_c}{\mathcal{E}_c}\}_{c=3}^n \end{pmatrix} \quad |B(\boldsymbol{\kappa})\rangle = \zeta \begin{pmatrix} 0 \\ 1 \\ \{-\frac{g_c}{\mathcal{E}_c}\}_{c=3}^n \end{pmatrix}. \quad (67)$$

These are manifestly *continuous and differentiable* at  $\boldsymbol{\kappa} \rightarrow \mathbf{0}$ , meaning that the vector bundle spanned by the two principal bands is continuous and differentiable at the principal node. We find that the Euler connection and the Euler form to the leading order in  $\kappa$  in the *rotated basis* are

$$\tilde{\mathbf{a}} = \langle A | \nabla B \rangle = \sum_{c=3}^n \frac{\zeta (\alpha_c \kappa_x + \beta_c \kappa_y)}{\mathcal{E}_c^2} (\gamma_c, \delta_c) \quad (68)$$

and

$$\begin{aligned} \tilde{\text{Eu}} &= \langle \partial_1 A | \partial_2 B \rangle - \langle \partial_2 A | \partial_1 B \rangle \\ &= -\zeta \sum_{c=3}^n \frac{1}{\mathcal{E}_c^2} (\beta_c \gamma_c - \alpha_c \delta_c) \end{aligned} \quad (69)$$

which are both perfectly regular for  $\boldsymbol{\kappa} \rightarrow \mathbf{0}$ . In particular, the result in Eq. (69) exactly reproduces the  $\phi$ -*independent* contribution to Eq. (62). Moreover, one can show that Stokes' theorem applies, i.e. the surface integral of  $\tilde{\text{Eu}}$  is exactly cancelled by the boundary integral of  $\tilde{\mathbf{a}}$ . Therefore, in the rotated basis the Euler class  $\tilde{\chi}(\mathcal{D})$  cannot be meaningfully defined for a manifold  $\mathcal{D}$  with a boundary [see Sec. F for definition]. Euler class defined this way would always be zero.

We now translate the results in Eqs. (68) and (69) to the eigenstates basis, which corresponds to a gauge transformation using  $X^\top$  from Eq. (66). We must keep in mind that this is a large gauge transformation, i.e. it introduces a singular winding at one point (at the principal node), but it is smooth elsewhere. First, it follows from Eq. (25) that everywhere outside the principal node we must have  $\text{Eu} = \tilde{\text{Eu}}$ . Since the latter is continuous, the correct functional form of the Euler form in the eigenstate basis is

$$\text{Eu} = -\zeta \sum_{c=3}^n \frac{1}{\mathcal{E}_c^2} (\beta_c \gamma_c - \alpha_c \delta_c), \quad (70)$$

which can be analytically continued to the point  $\kappa = 0$ .

A more dramatic change occurs when applying Eq. (20) to transform the connection  $\tilde{\mathbf{a}}$  to the eigenstate basis. First, we derive

$$X^\top dX = \frac{d\phi}{2} \begin{pmatrix} 0 & \mp\zeta \\ \pm\zeta & 0 \end{pmatrix} \quad (\text{for } \kappa \neq 0), \quad (71)$$

from where  $\text{Pf}(X^\top dX) = \mp \frac{1}{2} \zeta d\phi$  everywhere outside the principal node. From  $\phi = \arctan(\frac{\kappa_y}{\kappa_x})$  we obtain

$$d\phi = \frac{-\kappa_y d\kappa_x + \kappa_x d\kappa_y}{\kappa_x^2 + \kappa_y^2} = \frac{-\sin \phi}{\kappa} d\kappa_x + \frac{\cos \phi}{\kappa} d\kappa_y. \quad (72)$$

Note that the term  $\text{Pf}(X^\top dX)$  diverges for  $\kappa \rightarrow 0$  (consequence of  $X$  being a *large* gauge transformation around the principal node), and therefore it completely overshadows the expression in Eq. (68) which vanishes completely for  $\kappa \rightarrow 0$ . Therefore, according to Eq. (20), the Euler connection in the eigenstate basis to the leading order in  $\kappa$  equals

$$\mathbf{a} = -X^\top dX = \frac{\pm\zeta}{2\kappa} (-\sin \phi, \cos \phi), \quad (73)$$

which agrees with our result in Eq. (61).

It is worth to emphasize that the finite quantized value of  $\chi(\mathcal{D}^\epsilon)$  for the disk enclosing a principal node in the eigenstate basis comes entirely from the connection on the boundary  $\partial\mathcal{D}^\epsilon$  and is inherited from the large gauge transformation from the continuous basis. This is compatible with our claim, mentioned in the beginning of Sec. E, that it is expected that the eigenstate basis carries the topological information about the principal nodes on a patch, while the continuous basis does not have access to this information. Nevertheless, if one considers a *closed* base manifold  $B$  (e.g. the whole BZ torus), then  $\partial B = \emptyset$ , and only the surface integral of the Euler form contributes to the Euler class  $\chi(B)$ . Since Euler form is the same both for the eigenstate basis and the continuous basis, the value of Euler class on a *closed* manifold is quantized for both computations.

## F. Euler class for manifolds with a boundary

In this section, we generalize the notion of Euler class of a pair of principal bands in two important ways. First, we consider a base manifold *with a boundary*. Throughout the discussion, we explicitly assume that the manifold is topologically a *disc* (denoted  $\mathcal{D}$ ), which has boundary homeomorphic to a circle ( $\partial\mathcal{D} \simeq S^1$ ). Nevertheless, most of the presented results readily generalize to arbitrary manifolds with a boundary as long as the vector bundle spanned by the principal bands remains orientable. Second, we admit the occurrence of principal nodes inside the base manifold. Crucially, to obtain useful information from such a generalization, it is essential to *adopt*

the *eigenstate basis*. We find that the value of the Euler class on a disc  $\mathcal{D}$ , denoted  $\chi(\mathcal{D})$ , indicates whether the collection of principal nodes can annihilate inside  $\mathcal{D}$ .

The first generalization is straightforward. If there are no band nodes in  $\mathcal{D}$ , then the eigenstate basis is continuous. Therefore, Stokes' theorem guarantees that

$$\chi(\mathcal{D}) = \frac{1}{2\pi} \left( \int_{\mathcal{D}} \text{Eu} - \oint_{\partial\mathcal{D}} \mathbf{a} \right) = 0 \quad (\text{if no nodes in } \mathcal{D}) \quad (74)$$

is invariant. Let us further assume the presence of principal nodes in  $\mathcal{D}$  (but no adjacent nodes as we want the bundle to remain orientable). We proved in the second part of Sec. E that the vector bundle spanned by the two principal bands is continuous everywhere, including at the nodes. However one has to depart from the eigenstate basis to reveal this fact, and instead has to consider the continuous “mixed” basis, cf. Eqs. (64–69). In the continuous basis, Stokes' theorem applies, which implies the validity of Eq. (74) even in the presence of principal nodes. One concedes that the vector bundle spanned by the two principal bands on a disc cannot support a non-trivial topological invariant.

However, one should keep in mind the *physical realization* of the vector bundle as a pair of energy bands that are non-degenerate away from the band nodes. This interpretation equips the bundle with a canonical basis, namely the *eigenstate basis* discussed at length in Sec. E (cf. the comments on *flag bundle* description in Sec. E1). Therefore, one should only consider deformations of the vector bundle which preserve this additional structure. Indeed, we show below that such a constraint allows for a subtly modified definition of  $\chi(\mathcal{D})$ , which constitutes a *half-integer* topological invariant.

To develop the generalization of the Euler class, one should first recognize that each principal node is associated with a Dirac string [30]. Returning back to Eqs. (50–53), we observe that the continuous real gauge for eigenstates near a principal node is *double-valued*, namely the overall sign of both states is reversed if we increase  $\phi \mapsto \phi + 2\pi$ . Therefore, any *single-valued* gauge must necessarily exhibit a discontinuity – the Dirac string – across which both principal states flip sign. Each principal node must constitute the end-point of a Dirac string. Furthermore, since away from band nodes the eigenstates basis is continuous, there are no other end-points for Dirac strings. Therefore, in the eigenstate basis there is a *one-to-one correspondence* between the principal nodes and the end-points of Dirac strings. From this perspective, the gauge transformation to the continuous basis, analyzed in Eqs. (50–53), can be understood as creation of a new Dirac string that *exactly compensates* the “physical” Dirac string present in the eigenstate basis. This explains the difference between the Euler connection computed in the two different bases in Sec E.

The exact position of the Dirac strings (i.e. besides their fixed end-points) is arbitrary, and should not have any bearing on physical observables. Indeed, we find

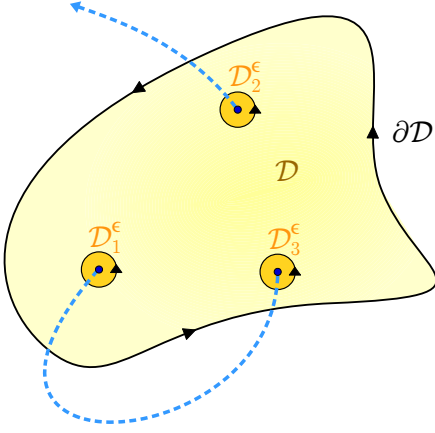


FIG. S-2. Illustration of the use of Stokes' theorem as discussed in the text. Region  $\mathcal{D}$  is the disc on which we study the real orientable vector bundle, and the blue dots are the principal nodes. We apply Stokes' theorem to  $\mathcal{D} \setminus \cup_{\alpha} \mathcal{D}_{\alpha}^{\epsilon}$ , i.e. to the region with tiny discs around the nodes cut out. The blue dashed lines represent Dirac strings. Only the end-points of Dirac strings are physically meaningful. In the case of the eigenstate basis the Dirac string end-points coincide with principal nodes, whereas a gauge transformation that regularizes the nodes creates a new Dirac string that exactly compensates the singular behavior.

that both Euler connection and Euler form are *continuous* at a Dirac string. This readily follows from the transformation rules presented in Sec. C, namely we see from Eqs. (20) and (25) that the orientation-preserving gauge transformation  $X = -1$  ( $\det X = +1$ ) leaves both  $\text{Eu}(\mathbf{k})$  and  $\mathbf{a}(\mathbf{k})$  invariant. We conclude that the relation  $\text{Eu}(\mathbf{k}) = d\mathbf{a}(\mathbf{k})$  remains valid along Dirac strings, meaning that they are no obstructions for the use of Stokes' theorem. Therefore, the *only* obstructions for Stokes' theorem are the principal nodes themselves, since at their locations the derivatives of the principal eigenstates are not well defined and the Euler connection diverges, cf. Sec. E. We thus use Stokes' theorem to relate

$$2\pi\chi(\mathcal{D}) = \int_{\mathcal{D}} \text{Eu} - \oint_{\partial\mathcal{D}} \mathbf{a} \quad (75)$$

$$= \sum_{\alpha} \left( \int_{\mathcal{D}_{\alpha}^{\epsilon}} \text{Eu} - \oint_{\partial\mathcal{D}_{\alpha}^{\epsilon}} \mathbf{a} \right) \quad (76)$$

where the summation index  $\alpha$  indicates the principal nodes inside the region  $\mathcal{D}$ , and  $\mathcal{D}_{\alpha}^{\epsilon}$  is a disc with radius  $\epsilon$  centered at principal node  $\alpha$ .

To simplify Eq. (76), we proceed as follows. First, we found in Sec. E that Euler form is bounded near principal nodes, hence the integrals over  $\mathcal{D}_{\alpha}^{\epsilon}$  converge to 0 in the limit  $\epsilon \rightarrow 0$ . Furthermore, it follows from Eq. (61) that  $\mathbf{a} \cdot d\mathbf{k} = \mp \frac{1}{2} \zeta d\phi$  for  $\epsilon \rightarrow 0$ , which integrates to  $\mp \zeta \pi$  on  $\partial\mathcal{D}_{\alpha}^{\epsilon}$ . Plugging this result into Eq. (76), we find

$$\chi(\mathcal{D}) = \frac{\zeta}{2} \sum_{\alpha} w_{\alpha} \quad (77)$$

where  $w_{\alpha} = \pm 1$  describes the *winding number* of the

principal node, while  $\zeta = \pm 1$  is the global orientation of the vector bundle. The result in Eq. (77) proves that  $\chi(\mathcal{D})$  of the orientable bundle spanned by the two principal states on region  $\mathcal{D}$  with a boundary is a *half-integer topological invariant* if one works in the eigenstate basis.

Let us conclude the section with several remarks:

1. Note that Eq. (77) expresses  $\chi(\mathcal{D})$  as a sum of  $\pm \frac{1}{2}$  quanta carried by the principal nodes. If the nodes were able to annihilate inside  $\mathcal{D}$ , then we would be left with a nodeless region, for which we proved in Eq. (74) that  $\chi(\mathcal{D}) = 0$ . Therefore, non-trivial value  $\chi(\mathcal{D}) \neq 0$  is an obstruction for annihilating the principal nodes inside  $\mathcal{D}$ .
2. The two admissible values of a winding number  $w_{\alpha} = \pm 1$  are reminiscent of the frame-rotation angle associated with the node being either  $+\pi$  or  $-\pi$ . We prove in Sec. G that this intuition is correct, i.e. the two quantities are in an exact one-to-one correspondence.
3. One should take into account that Eq. (77) is not as useful in practice as it appears! To make sure that we take the same orientation of the vector bundle at all principal nodes, it is necessary to know the bundle along some trajectories connecting the principal nodes. To avoid this extra work, our numerical algorithm for computing  $\chi(\mathcal{D})$ , presented in Sec. H is based on directly implementing Eq. (75).
4. In the presence of additional *adjacent* nodes, the vector bundle ceases to be orientable, and the relative orientation of two principal nodes depends on the specific choice of trajectory connecting them. This foreshadows the non-Abelian conversion of band nodes which we discuss in the main text of the manuscript. This “braiding” phenomenon is more carefully exposed in the next section.

## G. Non-Abelian frame-rotation charge

In this section, we review the original derivation of the non-Abelian exchange of band nodes in  $\mathbf{k}$ -space, which was obtained by Ref. [25] using homotopy theory [65]. We subsequently show that the same non-Abelian behavior is reproduced by considering the Euler class on manifolds with a boundary, as has been defined in Sec. F. Similar observations on a less formal level were also made by Ref. [30]. The exact correspondence between the two approaches provides a proof that the two distinct mathematical descriptions of the braiding phenomena (homotopy theory vs. cohomology classes) are two windows into the same underlying topological structure.

In the homotopic description, one begins with identifying the space  $M_N$  of  $N$ -band real symmetric matrices that do not exhibit level degeneracy. This corresponds to Bloch Hamiltonians at momenta lying away

from band nodes. With this assumption, we can uniquely order *all* eigenstates of  $H(\mathbf{k})$  according to increasing energy into an  $O(N)$  matrix  $\{|u^a(\mathbf{k})\rangle\}_{a=1}^N \equiv F(\mathbf{k})$ , which can be interpreted as an *orthonormal*  $N$ -frame. We further adjust band energies  $\{\varepsilon^a(\mathbf{k})\}_{a=1}^N$  to some standard values (e.g.  $\varepsilon^a = a$ ) while preserving their ordering. The space of such *spectrally normalized* Hamiltonians is  $M_N = O(N)/\mathbb{Z}_2^N$ , where the quotient corresponds to flipping the overall sign of any of the  $N$  eigenvectors, which leaves the spectrally normalized Hamiltonian  $H(\mathbf{k}) = \sum_{a=1}^N |u^a(\mathbf{k})\rangle \varepsilon^a \langle u^a(\mathbf{k})|$  invariant. Band nodes correspond to obstructions for a unique ordering of bands by energy, and thus induce discontinuities of frame  $F(\mathbf{k})$ .

To describe the band nodes, we study the topology of space  $M_N$ . Since there are  $2^N$  different frames (corresponding to the quotient  $\mathbb{Z}_2^N$ ) which all represent the same Hamiltonian, the following scenario is possible: We start at some point  $\mathbf{k}_0$ , and we follow the continuously rotating frame  $F(\mathbf{k})$  that encodes the Hamiltonian  $H(\mathbf{k})$  along  $\mathbf{k} \in \gamma$ , until we reach again  $\mathbf{k}_0$  as the final point. Comparing the initial vs. the final frame at  $\mathbf{k}_0$ , we may find that they are two *different* of the  $2^N$  frames representing the same Hamiltonian  $\mathcal{H}(\mathbf{k}_0)$ . We say that the Hamiltonian underwent a non-trivial *frame rotation*, which represents a non-trivial closed path inside  $M_N$ . For example, we know from Secs. E and F that a band node leads to a  $\pi$ -rotation of the frame by  $X = (1, \dots, 1, -1, -1, 1, \dots, 1)$ , where the two negative entries correspond to the two bands forming the node. More generally, since the handedness of the frame cannot change under the continuous evolution along  $\gamma$ , only  $\frac{1}{2} \cdot 2^N = 2^{N-1}$  of the elements with  $\det X = +1$  can actually be reached. Since the frame rotation is quantized to a discrete set of elements, it constitutes a topological invariant of the Hamiltonian  $H(\mathbf{k})$  along path  $\gamma$ , which cannot change under continuous deformations as long as the spectrum along  $\gamma$  remains non-degenerate.

To explain the origin of the non-Abelian exchange of band nodes, let us briefly focus on models with  $N = 3$  bands. The same discussion also applies to *any three consecutive bands* in models with  $N \geq 3$  bands. A node formed by the lower (upper) two bands corresponds to a  $\pi$ -rotation in the first (last) two coordinates, i.e.  $X_{12} = \text{diag}(-1, -1, +1)$  [ $X_{23} = \text{diag}(+1, -1, -1)$ ]. A path that encloses *one of each* species of nodes is associated with total frame rotation  $X_{13} = \text{diag}(-1, +1, -1)$ . However, while the geometric transformations

$$X_{12} \cdot X_{23} = X_{23} \cdot X_{12} \quad (78)$$

clearly commute, the continuous *paths* in  $SO(3)$  that realize the left-hand vs. the right-hand side of Eq. (78) are topologically *distinct*. To see this, recall that  $SO(3)$  can be visualized as a solid three-dimensional ball with radius  $\pi$  and with antipodal points on the surface being pairwise identified. This relation is achieved by mapping  $R(\alpha; \mathbf{n})$  (i.e. a clockwise rotation by angle  $0 \leq \alpha \leq \pi$  around axis given by unit vector  $\mathbf{n}$ ), with a point inside

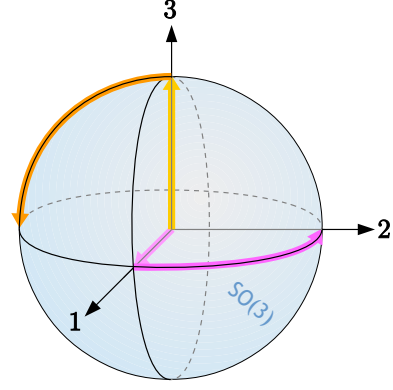


FIG. S-3. Geometry of rotations in three dimensions. If we represent clockwise rotation by angle  $0 \leq \alpha \leq \frac{\pi}{2}$  around unit vector  $\mathbf{n}$  by point with position  $\mathbf{r} = \alpha \mathbf{n}$ , then  $SO(3)$  looks like a ball with radius  $\pi$  and with antipodal points on the surface identified. The orange vs. the pink trajectory represent two ways of composing a  $\pi$  rotation around axis 1 with a  $\pi$  rotation around axis 3. The two trajectories cannot be continuously deformed into one another, i.e. they are topologically distinct. From this observation we deduce that topological charges associated with band nodes in consecutive band gaps do not commute with each other.

the ball at position  $\mathbf{r} = \alpha \mathbf{n}$ . Then rotating first by  $\pi$  around axis 1 and then by  $\pi$  around axis 3 traces the pink path in Fig. S-3, while performing the two rotations in reverse order produces the orange path in Fig. S-3, which follows from

$$R(\alpha; \hat{\mathbf{e}}_3) \cdot R(\pi; \hat{\mathbf{e}}_1) = R(\pi; +\cos \frac{\alpha}{2} \hat{\mathbf{e}}_1 + \sin \frac{\alpha}{2} \hat{\mathbf{e}}_2) \quad (79)$$

$$R(\alpha; \hat{\mathbf{e}}_1) \cdot R(\pi; \hat{\mathbf{e}}_3) = R(\pi; +\cos \frac{\alpha}{2} \hat{\mathbf{e}}_3 - \sin \frac{\alpha}{2} \hat{\mathbf{e}}_2) \quad (80)$$

where  $\hat{\mathbf{e}}_i$  indicates the unit vector directed along axis  $i \in \{1, 2, 3\}$ . The two paths in Fig. S-3 both connect the center of the ball to the  $\pi$ -rotation around axis 2. However, these paths cannot be continuously deformed into each other, i.e. they are topologically distinct. This ultimately follows from the fact that  $SO(3)$  is not a simply connected space. As a consequence, the ordering of the group elements from the  $\mathbb{Z}_2^N$  quotient matters, and the topological charges associated with a pair of band nodes inside consecutive band gaps *do not commute*!

A careful analysis [25] reveals that the algebra of closed paths in space  $M_N = O(N)/\mathbb{Z}_2^N$  is governed by group  $Q_N$  (called “Salingaros group” [71]) which is uniquely characterized by the following four conditions [72]. We use  $+1$  to indicate the identity element.

- (i) There is a unique element  $-1 \neq +1$  which has the property  $(-1)^2 = +1$ .
- (ii) For each band gap  $1 \leq G \leq (N-1)$  there is an associated element  $g_G$  such  $(g_G)^2 = -1$ .
- (iii)  $g_G \cdot g_{G'} = \epsilon g_{G'} \cdot g_G$ , where  $\epsilon = -1$  (anticommute) if  $|G - G'| = 1$  and  $\epsilon = +1$  (commute) otherwise.
- (iv) All elements of  $Q_N$  can be expressed by composing elements  $g_G$ .



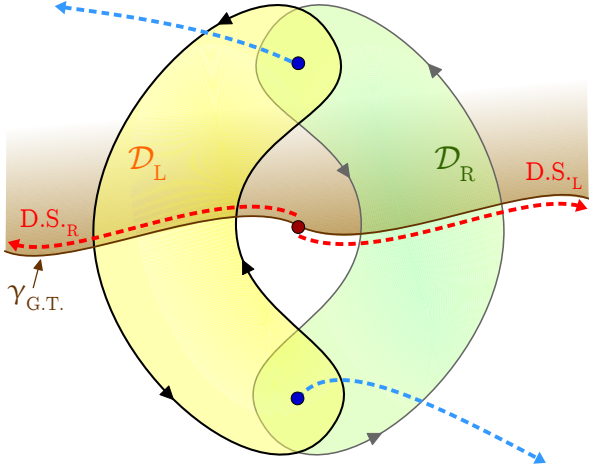


FIG. S-4. We consider two principal nodes (blue dots) near an adjacent node (red dot). Principal nodes are end-points of Dirac strings associated with a proper gauge transformation  $X = -1$  (dashed blue lines), which does not affect the continuity of Euler connection and Euler form of the vector bundle spanned by the two principal bands. On the other hand, the adjacent node is an end-point of a Dirac string associated with an improper transformation  $X = \pm\sigma_z$  (dashed red line), which reverses the orientation of the bundle. The yellow resp. the green disc  $\mathcal{D}_{L,R}$  correspond to two topologically different coverings of the principal nodes, for which the bundle can be made orientable by choosing an appropriate position of the red Dirac string (indicated by D.S.L resp. D.S.R). The two gauges are related by a gauge transformation which has an orientation-reversing discontinuity along  $\gamma_{G.T.}$  (solid brown line). This gauge transformation reverses the orientation of the bundle near one of the nodes, thus flipping the relative contribution of the two nodes to the sum in Eq. (77).

The element  $-1$  corresponds to a  $2\pi$  rotation (around any axis), and corresponds to the generator of the fundamental group  $\pi_1[\text{SO}(N)] = \mathbb{Z}_2$  [36]. Most interestingly, condition (iii) states that band nodes in consecutive band gaps carry *anticommuting charges*. This corresponds to the fact, visible in Fig. S-3, that

$$R(\pi, \hat{e}_3) \cdot R(\pi, \hat{e}_1) = \underbrace{R(2\pi, \hat{e}_2)}_{“-1”} \cdot R(\pi, \hat{e}_1) \cdot R(\pi, \hat{e}_3) \quad (81)$$

if the rotations are interpreted as *paths* in  $\text{SO}(3)$ . The group  $\mathbb{Q}_3$  coincides with the quaternion group  $\{\pm 1, \pm i, \pm j, \pm k\}$ , therefore  $\mathbb{Q}_N$  for  $N \geq 3$  has been dubbed “generalized quaternions” by Ref. [25].

We finally show that the same anticommuting behaviour follows by studying the Euler form on manifolds with a boundary as defined in Sec. F. Our proof thus successfully bridges the homotopic description of Ref. [25] with the cohomological description proposed by Ref. [30] and further elaborated by the present work. To observe the non-trivial exchange, let us consider the situation, illustrated in Fig. S-4, with two principal nodes (blue dots) near an adjacent node (red dot). We know from Sec. F that principal nodes are end-points of Dirac strings carrying a proper gauge transformation  $X = -1$  on the two

principal bands (dashed blue lines). We showed in the same section that such a gauge transformation is harmless for the calculation of the Euler class. On the other hand, adjacent nodes are end-points of Dirac strings carrying an *improper* gauge transformation  $X = \pm\sigma_z$ , which flips the sign of *just one* of the principal bands. Therefore, the bundle spanned by the two principal bands is non-orientable on regions containing such “adjacent” Dirac strings. Especially, an annulus enclosing the adjacent node is traversed by such a Dirac string for any single-valued gauge of the eigenstate basis, i.e. the bundle spanned by the principal bands is non-orientable on such an annulus.

Nevertheless, the total Euler class of the two principal nodes can still be calculated, provided that one covers the nodes with a disc lying to the side of the adjacent node. We show in Fig. S-4 two such discs, labelled  $\mathcal{D}_{L,R}$ , which lie to the left (yellow) resp. to the right (green) of the adjacent node. Both discs admit a gauge with a well-defined orientation of the bundle, which is achieved by appropriately positioning the adjacent Dirac string (dashed red lines D.S.L resp. D.S.R) such that it lies *outside* of the corresponding disc. Importantly, these two gauges are related by a gauge transformation that has a discontinuity along path  $\gamma_{G.T.} = \text{D.S.L} \cup \text{D.S.R}$  (solid brown path in Fig. S-4). This gauge transformation rotates D.S.L into D.S.R (and vice versa), and is simply equal to  $X = 1$  on one side and to  $X = \pm\sigma_z$  on the other side of the path  $\gamma_{G.T.}$ . Such a gauge transformation necessarily reverses the orientation of the bundle at *exactly one* of the two principal nodes. It follows that the relative contribution of the two principal nodes to the sum in Eq. (77) is *reversed* due to the reversed orientation  $\zeta$  near one of the nodes. Therefore, if the contributions of the two nodes to the Euler class cancel on  $\mathcal{D}_L$  [e.g.  $\chi(\mathcal{D}_L) = \frac{1}{2} - \frac{1}{2} = 0$ ], then the Euler class is automatically non-trivial on  $\mathcal{D}_R$  [corresponding to  $\chi(\mathcal{D}_R) = \pm(\frac{1}{2} + \frac{1}{2}) = \pm 1$ ]. Following the discussion at the end of Sec. F, the two principal nodes annihilate if brought together along a trajectory inside  $\mathcal{D}_L$ , but are incapable to annihilate if brought together along a trajectory inside  $\mathcal{D}_R$ . We thus conclude that the anticommutation relation in Eq. (81) [resp. in axiom (iii) on the previous page] is exactly reproduced by the behaviour of Euler class on manifolds with a boundary.

## H. Numerical calculation of the Euler form.

To test the presented theory numerically, we have implemented a *Mathematica* code that takes as input (1) an  $N$ -band real-symmetric Bloch Hamiltonian, (2) two (consecutive) band indices, and (3) a rectangular region containing no adjacent nodes. The program outputs the Euler class on the defined region (with a boundary) for the selected pair of consecutive bands, by implementing Eq. (75) in the eigenstate basis. The code requires setting one hyper-parameter, namely the subdivision of the sides of rectangular region into a discrete set of points.

The code is briefly described below, and we have made it available online [41].

The code sequentially implements the following steps. It begins by initializing the input parameters. We define a Bloch Hamiltonian  $H[\mathbf{k}_1, \mathbf{k}_2]$ , two (consecutive) band indices **LowerBand** and **UpperBand** that label the two principal bands, and a rectangular domain  $k_1 \in [k1Min, k1Max]$ ,  $k_2 \in [k2Min, k2Max]$ . The code automatically extracts the total number of bands **TotalBands**. The labelling of the bands is such that the lowest-energy band is indexed by 1, and the highest-energy band is indexed by the value **TotalBands**. We further set the value of hyper-parameter **pts** which defines the discretization of the sides of the rectangular region into  $\mathbf{pts} \times \mathbf{pts}$  infinitesimal squares of size  $dk_1 \times dk_2$ , where  $dk_1 = (k1Max - k1Min)/pts$  and similarly for  $dk_2$ .

In the next stage, we prepare the data for the numerical calculation of the Euler connection and Euler form. We save the two numerically obtained principal eigenstates of the Hamiltonian at the regular mesh of points into a  $(\mathbf{pts} + 1) \times (\mathbf{pts} + 1) \times 2$  array called **AllStates**. Note that each entry of this array is itself an array of size **TotalBands**  $\times$  1 (i.e. a right eigenstate). However, numerical diagonalization of the Hamiltonian finds the principal bands with a random  $+/ -$  gauge, which has to be smoothed before computing the derivatives. Furthermore, we know from Sec. F that each principal node is a source of a Dirac string associated with a  $X = -1$  gauge transformation. This implies the absence of a single-valued continuous gauge on regions containing principal nodes. To deal with these two issues, the code proceeds as follows. First, it computes the Berry phase on each of the  $\mathbf{pts} \times \mathbf{pts}$  infinitesimal squares of the mesh, and stores the information in an array **Fluxes**. The default

value is  $+1$ , while squares containing a node are indicated by value  $-1$ . Positions of all the nodes are then extracted and saved as pairs of numbers in array **Nodes**. Knowing the position of all the principal nodes inside the region, the code follows a set of rules to fix the position of the Dirac strings. The chosen trajectories of the Dirac strings are saved in array **Strings**. The infinitesimal squares traversed by a Dirac string are characterized by **Strings**[[i,j]] =  $-1$ , else the default value is  $+1$ . Finally, the two principal states are gauged such that they vary smoothly away from the Dirac strings, while both of the states simultaneously flip sign across each Dirac string. This gauge is then used to update all the states stored in array **AllStates**.

In the final stage, the code takes the gauged eigenstates saved in **AllStates**, and uses them to compute Euler form inside the region and Euler connection on the boundary of the region. Following Eq. (75), these two quantities are integrated to obtain the Euler class on the rectangular region. The code computes Euler connection along the boundary by implementing Newton's method of finite differences to approximate the derivative in the expression for  $a(\mathbf{k})$  in Eq. (56). The numerical integral of the Euler connection is then saved as **EulerConnectionIntegral**.

To integrate the Euler form inside the rectangular region, we use the complexification discussed in Sec. C4. The complexified principal bands are stored in an  $(\mathbf{pts} + 1) \times (\mathbf{pts} + 1)$  array **ComplexifiedStates**. As discussed in Sec. C4, Euler form of the two principal bands is exactly reproduced as the Berry curvature of the complexified band. However, following Ref. [69], we directly compute the *flux* of the Euler form through each infinitesimal square, which exactly obeys

$$\begin{aligned} \text{Eu}(\mathbf{k}) dk_1 dk_2 &= \arg \text{tr} [P_{\mathbf{k}+dk_2} P_{\mathbf{k}+dk_1+dk_2} P_{\mathbf{k}+dk_1} P_{\mathbf{k}}] \\ &= \arg [\langle \psi_{\mathbf{k}} | \psi_{\mathbf{k}+dk_2} \rangle \langle \psi_{\mathbf{k}+dk_2} | \psi_{\mathbf{k}+dk_1+dk_2} \rangle \langle \psi_{\mathbf{k}+dk_1+dk_2} | \psi_{\mathbf{k}+dk_1} \rangle \langle \psi_{\mathbf{k}+dk_1} | \psi_{\mathbf{k}} \rangle] \end{aligned} \quad (82)$$

where  $P_{\mathbf{k}} = |\psi_{\mathbf{k}}\rangle \langle \psi_{\mathbf{k}}|$  is a projector onto the complexified state at momentum  $\mathbf{k}$ . With this trick, we elegantly avoid the accumulation of numerical errors in computing the derivatives of states in the right Eq. (56). For infinitesimal squares not traversed by a Dirac string we readily compute the Euler form via Eq. (82). For infinitesimal squares traversed by a Dirac string, we perform an extra gauge transformation to guarantee a continuous gauge on the four vertices of the square. Note also that the code is set to skip the computation of Euler form on infinitesimal squares containing the principal nodes (i.e. those with **Fluxes**[[i,j]] =  $-1$ ). We numerically integrate the Euler form by summing up the contributions from all infinitesimal squares, and the obtained approximation of the integral is saved as **EulerFormIntegral**. We finally output **EulerClass**, which is the difference of

**EulerFormIntegral** and **EulerConnectionIntegral** divided by  $2\pi$ , cf. the definition in Eq. (75).

To demonstrate the code performance, we consider the model in Eq. (1) of the main text for two values of  $t$ . First, for  $t = -2.5$ , the system exhibits two principal nodes near the *center* of the Brillouin zone. It is observed that these two nodes fail to annihilate at a collision for  $t = -2$ . To analyze the situation, we consider a square region  $k_1 \in [-1, 1]$  and  $k_2 \in [-1, 1]$ , which contains the two principal nodes and no adjacent nodes. The estimated value of Euler class is very close to  $-1$ , cf. Fig. S-5(a,b), consistent with the observed stability of the nodes. We contrast this to the situation with  $t = -5.5$ , when the region  $k_1 \in [\pi - 1, \pi + 1]$  and  $k_2 \in [\pi - 1, \pi + 1]$  contains no adjacent nodes but a pair of principal nodes, which have been pairwise created inside the region at an earlier

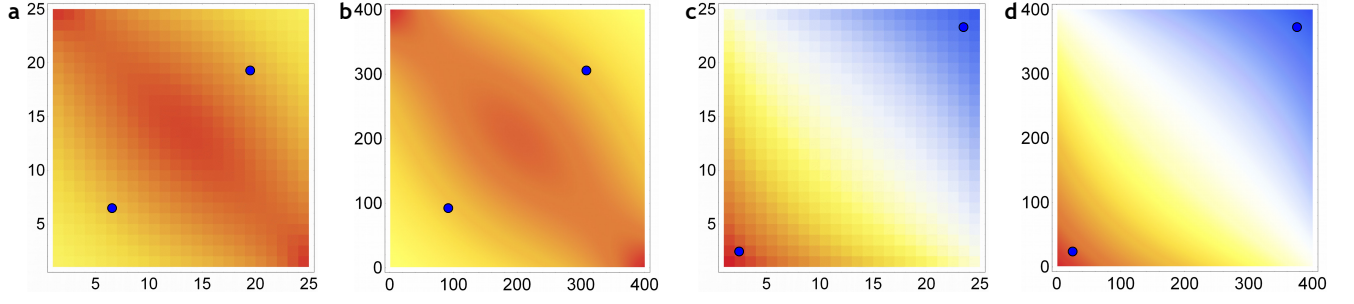


FIG. S-5. (a,b) Numerically computed Euler form for the model in Eq. (1) of the main text for  $t = -2.5$ . The considered region  $k_1 \in [-1, 1]$  and  $k_2 \in [-1, 1]$  contains two principal nodes (blue dots) and no adjacent nodes. The two panels differ in the mesh size,  $\text{pts} \in \{25, 400\}$ . The color scheme shows positive (negative) values in red (blue) tones, and white values in zero. The code adjusts the color scheme range to fully fit the computed range of  $|\text{Eu}(\mathbf{k})|$ . The estimated value of the Euler class is  $-0.984220$  in (a), and  $-0.999934$  in (b). This is numerical approximation of  $\chi(\mathcal{D}) = -1$ , implying that the two nodes cannot annihilate inside the region. The result is negative, because the positive area integral of  $\text{Eu}$  (note the red tones of the plots) is overcompensated by a larger negative boundary integral of  $\mathbf{a}$ . (c,d) Analogous data for  $t = -5.5$  and region  $k_1 \in [\pi - 1, \pi + 1]$  and  $k_2 \in [\pi - 1, \pi + 1]$ . For both choices of mesh, the computed Euler class is zero within  $\approx 10^{-7}$ , which implies that the nodes can annihilate inside the region.

time. In this case, the numerically computed Euler class is zero within  $\approx 10^{-7}w$ , cf. Fig. S-5(c,d), consistent with the fact that the nodes were pairwise created inside the region. It is worth to emphasize that the two principal nodes studied for  $t = -2.5$  resp. for  $t = -5.5$  are the same pair of nodes, but we have computed their Euler class inside different regions of the Brillouin zone. The Euler class on the two regions reaches different value, confirming that the capability of the principal nodes to annihilate depends on the choice of path used to bring them together.

### I. Frame rotations vs. flow of the Pfaffian

We now introduce yet another way of computing the frame-rotation charge (or Euler class) of two principal nodal points by making use of Wilson loops. Compared to Eq. (75) this approach has the advantage that it does not require the explicit construction of a smooth gauge for the eigenstates.

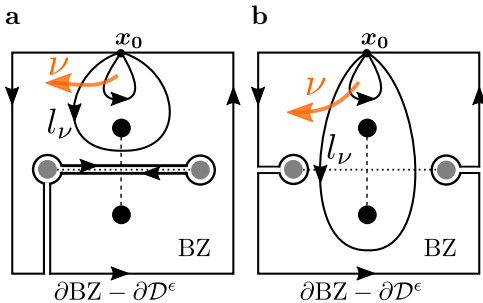


FIG. S-6. Two possible flows of a base loop ( $l_\nu$ ,  $\nu \in [0, 1]$ ) over the punctured Brillouin zone containing two principal nodes (black) and excluding two adjacent nodes (gray). The flow starts at a base point ( $l_0 = x_0$ ) and ends at the boundary  $l_1 = \partial\text{BZ} - \partial\mathcal{D}^\epsilon$ , with the orange arrow indicating the direction of the flow. Assuming that the pair of principal nodes were created first (along the dashed line between them), the Euler class is  $\chi[\text{BZ} - \mathcal{D}^\epsilon] = 0$  in case a, and  $\chi[\text{BZ} - \mathcal{D}^\epsilon] = 1$  in case b.

Adopting the real gauge for the eigenstates, the Wilson loop computed over the two-principal bands,

$$\mathcal{W}_l = \exp \left\{ \oint_l \mathcal{A}(\mathbf{k}) \cdot d\mathbf{l}(\mathbf{k}) \right\}, \quad (83)$$

is an element of the Lie group  $\text{SO}(2)$ . Therefore, every Wilson-loop matrix must correspond to a Wilson-loop Hamiltonian,  $\mathcal{W}_l = e^{i\mathcal{H}_{\mathcal{W}_l}}$ , where  $i\mathcal{H}_{\mathcal{W}_l}$  is an element of the Lie algebra  $\mathfrak{so}(2)$ , i.e. it is a real  $2 \times 2$  skew-symmetry matrix. We thus can parameterize the Wilson loop as  $\mathcal{W}_l = e^{\zeta(l)i\sigma_y}$ , with the function  $\zeta(l) \in \mathbb{R}$  obtained as the Pfaffian

$$\zeta(l) = \text{Pf} [i\mathcal{H}_{\mathcal{W}_l}] = \text{Pf} [\log \mathcal{W}_l]. \quad (84)$$

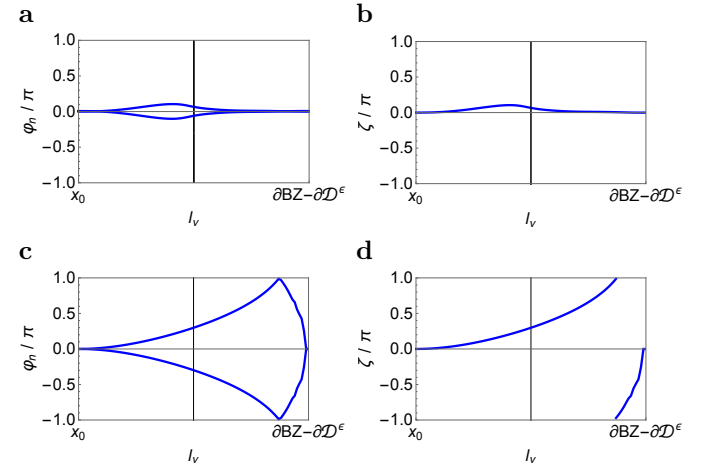


FIG. S-7. Wilson loop (a,c) and Pfaffian flow (b,d) over a punctured Brillouin zone containing two principal nodes, excluding two adjacent nodes corresponding to Fig. S-6a for a–b, and to Fig. S-6b for c–d. b The zero winding of the Pfaffian,  $\Delta\zeta = 0$ , indicates a trivial frame-rotation charge of the two principal nodes (i.e. zero Euler class on  $\text{BZ} - \mathcal{D}^\epsilon$ ). d The non-zero winding of the Pfaffian,  $\Delta\zeta/(2\pi) = 1$ , indicates a non-trivial frame-rotation charge of the two principal nodes (i.e. non-vanishing Euler class on  $\text{BZ} - \mathcal{D}^\epsilon$ ).

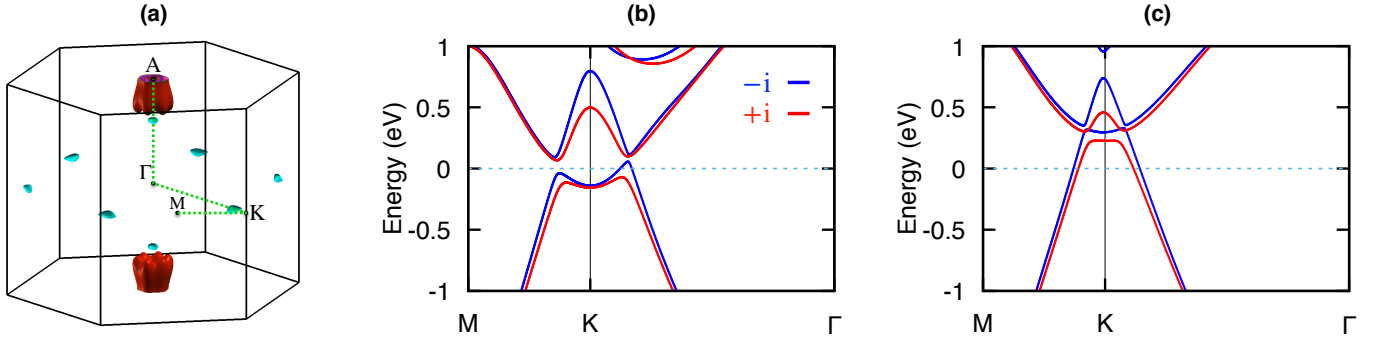


FIG. S-8. Fermi surface and band structures of ZrTe with and without strain. **a.** Fermi surface of ZrTe under ambient conditions, with pairs of Weyl nodes of opposite chirality located inside the cyan pockets close to  $k_z = 0$  plane. **b** and **c.** Band structures of ZrTe along high-symmetry lines of the Brillouin under 0% resp. under -2.6% uniaxial compression strain. Path M-K- $\Gamma$  is in the  $k_z = 0$  plane which is a mirror invariant plane. The mirror eigenvalues  $+i$  and  $-i$  are indicated as red and blue lines.

The Wilson loop is a periodic function of  $\zeta(l)$  modulo  $2\pi$ , and it changes continuously under smooth deformations of the base loop  $l$ . Therefore, the winding number of Wilson loop [29] is obtained as the winding number of  $\zeta(l)$  as the base loop flows over a closed two-dimensional manifold.

Since the nontrivial frame-rotation charge of a pair of principal nodes requires a braiding with adjacent nodes, we should generically consider the presence of adjacent nodes. Therefore, we assume that the principal two-band subspace is *not* separated by a band gap from the rest of the band structure. For this reason, we devise a flow of Wilson loop (resp. of the Pfaffian) over a punctured Brillouin zone  $\text{BZ} - \mathcal{D}^\epsilon$ , i.e. the Brillouin zone (BZ) from which we exclude the infinitesimal islands ( $\mathcal{D}^\epsilon$ ) surrounding the adjacent nodes. Fixing a base point ( $x_0$ ), we form oriented base loops ( $l_\nu$ ) within the punctured BZ. Then the flow is obtained by deforming the base loop smoothly over the punctured Brillouin zone ( $\nu \in [0, 1]$ ) from the base point ( $l_0 = x_0$ ) to the boundary  $l_1 = \partial\text{BZ} - \partial\mathcal{D}^\epsilon$ .

Assuming the presence of a pair of principal and of a pair of adjacent nodes, we can define two distinct flows, as illustrated in Fig. S-6. The dashed lines mark the origin of the creation of the pair of principal nodes (black) and adjacent nodes (gray). Assuming that the principal nodes were created first, we then know that the adjacent nodes can be annihilated along the dashed line between the two. From the computation of the Euler class in Eq. (75), we also know that the Euler class is zero (trivial frame-rotation charge) over the region  $\text{BZ} - \mathcal{D}^\epsilon$  of Fig. S-6a, i.e.  $\chi[\text{BZ} - \mathcal{D}^\epsilon] = 0$ , while it is finite (nontrivial frame-rotation charge) over the region  $\text{BZ} - \mathcal{D}^\epsilon$  of Fig. S-6b, i.e.  $\chi[\text{BZ} - \mathcal{D}^\epsilon] = 1$ .

Let us compare these predictions to the flow of the Wilson loop (and of the Pfaffian). To keep the analysis simple, we probe the scenario in Fig. S-6a for the model from the main text with  $t = 6$ , when the two adjacent nodes are located on top of each other at  $\Gamma$ , cf. Fig. 3c of the main text. We find (see Fig. S-7a for the Wilson-loop eigenvalues and Fig. S-7b for the Pfaffian) that the winding number is indeed trivial, consistent

with  $\chi[\text{BZ} - \mathcal{D}^\epsilon] = 0$ . In contrast, to probe the scenario from Fig. S-6b, we take the model from the main text with  $t = 2$ , when the two adjacent nodes are located on top of each other at M. In this case, we find (see Fig. S-7c and d) that there is a non-trivial winding number, consistent with  $\chi[\text{BZ} - \mathcal{D}^\epsilon] = 1$ . We thus conclude that the predictions based on combining the integrals of Euler form and of Euler connection are consistent with calculating the winding of the Wilson-loop Pfaffian.

## J. First-principle calculations

Our first-principles calculations are performed using VASP (Vienna *Ab initio* Simulation Package) [50, 73] which relies on all-electron projector augmented wave (PAW) basis sets [74] combined with the generalized gradient approximation (GGA) with exchange-correlation functional of Perdew, Burke and Ernzerhof (PBE) [75]. In order to better capture the correlation effects, Heyd-Scuseria-Ernzerhof (HSE06) screened hybrid functional [76] was used in all first-principle calculations. The cutoff energy for the plane wave expansion was set to 360 eV and a  $k$ -point mesh of  $12 \times 12 \times 12$  was adopted. The lattice constants are fully relaxed to  $a = 3.7807\text{\AA}$  and  $c = 3.8618\text{\AA}$  which are comparable with the experimental values  $a = 3.7706\text{\AA}$  and  $c = 3.8605\text{\AA}$  [77]. The WannierTools code [52] was used to search the nodal line and Weyl points in the Brillouin zone based on Wannier tight-binding model that was constructed by using the Wannier90 package [51] with Zr  $s, p, d$  and Te  $p$  atomic orbitals as projectors. Spin-orbit coupling (SOC) effect was considered.

The band structure along the path in the mirror invariant plane is shown in Fig. S-8. Weyl points and nodal lines are formed within two bands with different mirror eigenvalues. The Weyl points of ZrTe at ambient conditions are located inside the cyan pocket close to the mirror invariant plane.



- 
- [1] X.-G. Wen, *Adv. Phys.* **44**, 405 (1995).
- [2] M. Z. Hasan and C. L. Kane, *Rev. Mod. Phys.* **82**, 3045 (2010).
- [3] X.-L. Qi and S.-C. Zhang, *Rev. Mod. Phys.* **83**, 1057 (2011).
- [4] L. Fu and C. L. Kane, *Phys. Rev. Lett.* **100**, 096407 (2008).
- [5] A. Kitaev, *AIP Conf. Proc.* **1134**, 22 (2009).
- [6] S. Ryu, A. P. Schnyder, A. Furusaki, and A. W. W. Ludwig, *New J. Phys.* **12**, 065010 (2010).
- [7] L. Fu, *Phys. Rev. Lett.* **106**, 106802 (2011).
- [8] R.-J. Slager, A. Mesaros, V. Juričić, and J. Zaanen, *Nat. Phys.* **9**, 98 (2012).
- [9] X. Wan, A. M. Turner, A. Vishwanath, and S. Y. Savrasov, *Phys. Rev. B* **83**, 205101 (2011).
- [10] C. Fang, H. Weng, X. Dai, and Z. Fang, *Chin. Phys. B* **25**, 117106 (2016).
- [11] T. Bzdušek, Q.-S. Wu, A. Rüegg, M. Sigrist, and A. A. Soluyanov, *Nature* **538**, 75 (2016).
- [12] J. Kruthoff, J. de Boer, J. van Wezel, C. L. Kane, and R.-J. Slager, *Phys. Rev. X* **7**, 041069 (2017).
- [13] A. Bouhon and A. M. Black-Schaffer, *Phys. Rev. B* **95**, 241101 (2017).
- [14] H. C. Po, A. Vishwanath, and H. Watanabe, *Nat. Commun.* **8**, 50 (2017).
- [15] B. Bradlyn, L. Elcoro, J. Cano, M. G. Vergniory, Z. Wang, C. Felser, M. I. Aroyo, and B. A. Bernevig, *Nature* **547**, 298 (2017).
- [16] R.-J. Slager, *J. Phys. Chem. Solids* **128**, 24 (2019).
- [17] J. Höller and A. Alexandradinata, *Phys. Rev. B* **98**, 024310 (2018).
- [18] T. Zhang, Y. Jiang, Z. Song, H. Huang, Y. He, Z. Fang, H. Weng, and C. Fang, *Nature* **566**, 475 (2019).
- [19] G. Autes, Q. Wu, N. Mounet, and O. V. Yazyev, “Topomat: a database of high-throughput first-principles calculations of topological materials, materials cloud archive (2019),” .
- [20] V. Poenaru and G. Toulouse, *J. Phys. Lett.* **38**, 887 (1977).
- [21] G. E. Volovik and V. P. Mineev, *Zh. Eksp. Teor. Fiz* **72**, 2256 (1977).
- [22] L. A. Madsen, T. J. Dingemans, M. Nakata, and E. T. Samulski, *Phys. Rev. Lett.* **92**, 145505 (2004).
- [23] G. P. Alexander, B. G.-g. Chen, E. A. Matsumoto, and R. D. Kamien, *Rev. Mod. Phys.* **84**, 497 (2012).
- [24] K. Liu, J. Nissinen, R.-J. Slager, K. Wu, and J. Zaanen, *Phys. Rev. X* **6**, 041025 (2016).
- [25] Q. Wu, A. A. Soluyanov, and T. Bzdušek, *Science* **365**, 1273 (2019).
- [26] Y. Cao, V. Fatemi, S. Fang, K. Watanabe, T. Taniguchi, E. Kaxiras, and P. Jarillo-Herrero, *Nature* **556**, 43 (2018).
- [27] H. C. Po, L. Zou, T. Senthil, and A. Vishwanath, *Phys. Rev. B* **99**, 195455 (2019).
- [28] Z. Song, Z. Wang, W. Shi, G. Li, C. Fang, and B. A. Bernevig, *Phys. Rev. Lett.* **123**, 036401 (2019).
- [29] A. Bouhon, A. M. Black-Schaffer, and R.-J. Slager, *Phys. Rev. B* **100**, 195135 (2019).
- [30] J. Ahn, S. Park, and B.-J. Yang, *Phys. Rev. X* **9**, 021013 (2019).
- [31] J. Ahn, D. Kim, K. Youngkuk, and B.-J. Yang, *Phys. Rev. Lett.* **121**, 106403 (2018).
- [32] Y. X. Zhao and Y. Lu, *Phys. Rev. Lett.* **118**, 056401 (2017).
- [33] The Supplemental Material contains additional information about the (a) presented tight-binding models, (b) reality condition, (c) Euler form and Euler class, (d) their geometric interpretation in three-band models, (e) singularity of Euler form at principal nodes, (f) manifolds with boundary, (g) relation between Euler class and frame-rotation charge, (h) Euler form integration algorithm, (i) Wilson-flow algorithm, and (j) first-principles calculations.
- [34] M. V. Berry, *Proc. R. Soc. London, Se. A* **392**, 45 (1984).
- [35] Y. Zhang, Y.-W. Tan, H. L. Stormer, and P. Kim, *Nature* **438**, 201 (2005).
- [36] G. K. Francis and L. H. Kauffman, *Contemp. Math.* **169**, 261 (1994).
- [37] N. Johansson and E. Sjöqvist, *Phys. Rev. Lett.* **92**, 060406 (2004).
- [38] N. D. Mermin, *Rev. Mod. Phys.* **51**, 591 (1979).
- [39] T. Bzdušek and M. Sigrist, *Phys. Rev. B* **96**, 155105 (2017).
- [40] J. W. Milnor and J. D. Stasheff, *Ann. Math. Stud.* **76** (1975).
- [41] T. Bzdušek, “Euler class of a pair of energy bands on a manifold with a boundary,” ResearchGate (2019), publicly available Mathematica code.
- [42] X.-Q. Sun, S.-C. Zhang, and T. Bzdušek, *Phys. Rev. Lett.* **121**, 106402 (2018).
- [43] A. A. Soluyanov, D. Gresch, Z. Wang, Q.-S. Wu, M. Troyer, X. Dai, and B. A. Bernevig, *Nature* **527**, 495 (2015).
- [44] Z. Wang, D. Gresch, A. A. Soluyanov, W. Xie, S. Kushwaha, X. Dai, M. Troyer, R. J. Cava, and B. A. Bernevig, *Phys. Rev. Lett.* **117**, 056805 (2016).
- [45] S.-Y. Xu, N. Alidoust, G. Chang, H. Lu, B. Singh, I. Belopolski, D. S. Sanchez, X. Zhang, G. Bian, H. Zheng, M.-A. Hsuan, Y. Bian, S.-M. Huang, C.-H. Hsu, T.-R. Chang, H.-T. Jeng, A. Bansil, T. Neupert, V. N. Strocov, H. Lin, S. Jia, and M. Z. Hasan, *Sci. Adv.* **3**, e1603266 (2017).
- [46] Z. Zhu, G. W. Winkler, Q. Wu, J. Li, and A. A. Soluyanov, *Phys. Rev. X* **6**, 031003 (2016).
- [47] H. Weng, C. Fang, Z. Fang, and X. Dai, *Phys. Rev. B* **94**, 165201 (2016).
- [48] J. B. He, D. Chen, W. L. Zhu, S. Zhang, L. X. Zhao, Z. A. Ren, and G. F. Chen, *Phys. Rev. B* **95**, 195165 (2017).
- [49] J.-Z. Ma, J.-B. He, Y.-F. Xu, B. Q. Lv, D. Chen, W.-L. Zhu, S. Zhang, L.-Y. Kong, X. Gao, L.-Y. Rong, Y.-B. Huang, P. Richard, C.-Y. Xi, E. S. Choi, Y. Shao, Y.-L. Wang, H.-J. Gao, X. Dai, C. Fang, H.-M. Weng, G.-F. Chen, T. Qian, and H. Ding, *Nat. Phys.* **14**, 349 (2018).
- [50] G. Kresse and J. Furthmüller, *Phys. Rev. B* **54**, 11169 (1996).
- [51] A. A. Mostofi, J. R. Yates, G. Pizzi, Y.-S. Lee, I. Souza, D. Vanderbilt, and N. Marzari, *Comp. Phys. Commun.* **185**, 2309 (2014).
- [52] Q. Wu, S. Zhang, H.-F. Song, M. Troyer, and A. A. Soluyanov, *Comp. Phys. Commun.* **224**, 405 (2018).
- [53] S.-D. Guo, Y.-H. Wang, and W.-L. Lu, *New J. Phys.* **19**,

- 113044 (2017).
- [54] E. J. Sie, C. M. Nyby, C. Pemmaraju, S. J. Park, X. Shen, J. Yang, M. C. Hoffmann, B. Ofori-Okai, R. Li, A. H. Reid, *et al.*, **Nature** **565**, 61 (2019).
  - [55] T. Li, L. Duca, M. Reitter, F. Grusdt, E. Demler, M. Endres, M. Schleier-Smith, I. Bloch, and U. Schneider, **Science** **352**, 1094 (2016).
  - [56] F. Wilczek and A. Zee, **Phys. Rev. Lett.** **52**, 2111 (1984).
  - [57] N. Fläschner, B. S. Rem, M. Tarnowski, D. Vogel, D.-S. Lühmann, K. Sengstock, and C. Weitenberg, **Science** **352**, 1091 (2016).
  - [58] O. Zilberberg, S. Huang, J. Guglielmon, M. Wang, K. P. Chen, Y. E. Kraus, and M. C. Rechtsman, **Nature** **553**, 59 EP (2018).
  - [59] D. B. Litvin, *Magnetic Group Tables* (International Union of Crystallography, 2013).
  - [60] C. J. Bradley and A. P. Cracknell, *The Mathematical Theory of Symmetry in Solids* (Oxford University Press, 1972).
  - [61] E. P. Wigner, **Journal of Mathematical Physics** **1**, 409 (1960).
  - [62] R. A. Horn and C. R. Johnson, *Matrix analysis* (Cambridge University Press, Cambridge, 2012).
  - [63] K. D. Ikramov, **Comput. Math. Math. Phys.** **52**, 1 (2012).
  - [64] H. A. Kramers, **Koninkl. Ned. Akad. Wetenschap., Proc.** **33**, 959 (1930).
  - [65] M. Nakahara, *Geometry, Topology and Physics* (Taylor & Francis Group, Abingdon, 2003).
  - [66] A. Hatcher, “**Vector Bundles and K-Theory**,” (unpublished).
  - [67] S.-s. Chern, **Ann. Math.** **46**, 674 (1945).
  - [68] A. Hatcher, *Algebraic Topology* (Cambridge University Press, Cambridge, 2002).
  - [69] T. Fukui, Y. Hatsugai, and H. Suzuki, **J. Phys. Soc. Jpn.** **74**, 1674 (2005).
  - [70] W. Fulton, *Intersection Theory* (Springer-Verlag, Berlin, 1984).
  - [71] N. Salingaros, **J. Math. Phys.** **25**, 738 (1983).
  - [72] A. Tiwari and T. Bzdušek, ArXiv e-prints (2019), [arXiv:1903.00018](https://arxiv.org/abs/1903.00018).
  - [73] G. Kresse and D. Joubert, **Phys. Rev. B** **59**, 1758 (1999).
  - [74] P. E. Blöchl, **Phys. Rev. B** **50**, 17953 (1994).
  - [75] J. P. Perdew, K. Burke, and M. Ernzerhof, **Phys. Rev. Lett.** **77**, 3865 (1996).
  - [76] A. V. Krukau, O. A. Vydrov, A. F. Izmaylov, and G. E. Scuseria, **The Journal of Chemical Physics** **125**, 224106 (2006), <https://doi.org/10.1063/1.2404663>.
  - [77] G. Örlygsson and B. Harbrecht, **Zeitschrift für Naturforschung - Section B Journal of Chemical Sciences** **54**, 1125 (1999).